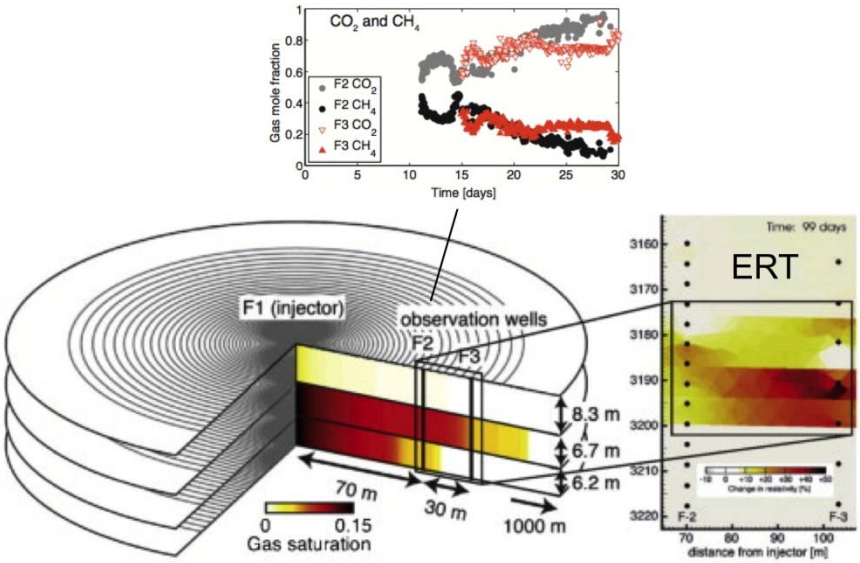

Coupled Inversion of Hydrological and Geophysical Data for Improved Prediction of Subsurface CO_2 Migration

28 January 2016

Office of Fossil Energy

NRAP-TRS-III-004-2016

Disclaimer

This report was prepared as an account of work sponsored by an agency of the United States Government. Neither the United States Government nor any agency thereof, nor any of their employees, makes any warranty, express or implied, or assumes any legal liability or responsibility for the accuracy, completeness, or usefulness of any information, apparatus, product, or process disclosed, or represents that its use would not infringe privately owned rights. Reference therein to any specific commercial product, process, or service by trade name, trademark, manufacturer, or otherwise does not necessarily constitute or imply its endorsement, recommendation, or favoring by the United States Government or any agency thereof. The views and opinions of authors expressed therein do not necessarily state or reflect those of the United States Government or any agency thereof.

This report has been reviewed by Lawrence Berkeley National Laboratory and the National Energy Technology Laboratory approved for public release.

Cover Illustration: Schematic of time-lapse hydrological and geophysical monitoring data in a coupled hydrological-geophysical inverse modeling framework for improved monitoring and prediction of subsurface CO_2 migration.

Suggested Citation: Kowalsky, M. B.; Doetsch, J.; Commer, M.; Finsterle, S.; Doughty, C.; Zhou, Q.; Ajo-Franklin, J.; Birkholzer, J.; Daley, T. *Coupled Inversion of Hydrological and Geophysical Data for Improved Prediction of Subsurface CO_2 Migration*; NRAP-TRS-III-004-2016; NRAP Technical Report Series; U.S. Department of Energy, National Energy Technology Laboratory: Morgantown, WV, 2016; p 56.

An electronic version of this report can be found at:

http://www.netl.doe.gov/research/on-site-research/publications/featured-technical-reports

https://edx.netl.doe.gov/nrap/

Coupled Inversion of Hydrological and Geophysical Data for Improved Prediction of Subsurface CO_2 Migration

Michael B. Kowalsky[1], Joseph Doetsch[1,2], Michael Commer[1], Stefan Finsterle[1], Christine Doughty[1], Quanlin Zhou[1], Jonathan Ajo-Franklin[1], Jens Birkholzer[1], Thomas Daley[1]

[1]Lawrence Berkeley National Laboratory, 1 Cyclotron Road, Berkeley, CA 94720

[2]Aarhus University, DK-8000 Aarhus, Denmark

NRAP-TRS-III-004-2016

Level III Technical Report Series

28 January 2016

This page intentionally left blank.

Table of Contents

EXECUTIVE SUMMARY **1**

1. INTRODUCTION **4**

2. METHODS **6**
2.1 COUPLED HYDROLOGICAL-GEOPHYSICAL INVERSION FRAMEWORK 6
2.2 HYDROLOGICAL FORWARD MODELING 7
2.3 GEOPHYSICAL FORWARD MODELING 8
2.4 DEMONSTRATION FOR SEISMIC AND HYDROLOGICAL MEASUREMENTS 8

3. CRANFIELD STUDY **12**
3.1 FIELD SITE AND CO_2 INJECTION EXPERIMENT 12
3.2 INVERSION COMPONENTS 19
3.3 ANALYSIS OF TIME-LAPSE ERT DATA 22
3.4 COUPLED HYDROLOGICAL-GEOPHYSICAL INVERSION RESULTS 29
3.5 DISCUSSION 39
3.6 CONCLUSIONS 40

4. REFERENCES **43**

This page intentionally left blank.

List of Figures

Figure 1: Schematic of the problem used to demonstrate coupled hydrological-geophysical modeling. 9

Figure 2: Example of measurements that can be modeled in a coupled hydrological-geophysical simulation. 10

Figure 3: 2-D hydrological model for Frio II experiment with overlapping geophysical grid for simulating seismic travel times. 11

Figure 4: Example of simulated and measured CO_2 saturation and seismic travel times. 11

Figure 5: (a) Location of the Cranfield site in Mississippi. (b) Photograph of site showing injection borehole 31F-1 (F1) and observation boreholes 31F-2 (F2) and 31F-3 (F3). 12

Figure 6: Select geophysical borehole logging data. 13

Figure 7: Gas composition monitoring data measured with a U-tube device in observation wells F2 and F3. 15

Figure 8: Seismic velocity distribution from inversion of baseline (pre-injection) crosswell data, and comparison of inversion with (smoothed) sonic logs at the three observation wells. 16

Figure 9: Inversion for CO_2-induced-changes in seismic velocity, from baseline to after nearly 10 months of injection, (a) using stochastic regularization to estimate a change in velocity at each point and (b) estimating only a single value for the change in velocity within the plume region. 17

Figure 10: Time series of electrical resistance measurements using various electrode combinations in wells F2 and F3, normalized by the pre-injection resistances. 19

Figure 11: Inversion of seismic and ERT data for changes in seismic velocity and resistivity from baseline to 9 months after the start of CO_2 injection. 23

Figure 12: Example time-lapse ERT inversions at 25 days and 99 days after the start of CO_2 injection. E 24

Figure 13: Change in resistivity, normalized by baseline resistivity, inferred from time-lapse ERT inversions. 26

Figure 14: Inversion for 3-D resistivity distribution, converted to CO_2 saturation as function of time. 27

Figure 15: Estimation of CO_2 saturation based on 2-D ERT inversion 28

Figure 16: Meshes for the flow and transport modeling in Sections 3.4.1 through 3.4.3. 30

Figure 17: CH_4 and CO_2 gas mole fraction and gas saturation as simulated by model M1 at day 13. 30

Figure 18: Measured and simulated CO_2 gas mole fraction in (a) F2 and (b) F3, as well as (c–e) inverted and simulated resistivity time series. 32

List of Figures (continued)

Figure 19: Comparison of additional field data (not used in inversion of this section) and simulation results using the final 3-D model from Section 3.4.2. 34

Figure 20: Field site and corresponding numerical grid used in Section 3.4.4 shown in its entirety and zoomed in around the wells 36

Figure 21: Computing times versus resources for a single forward simulation of the Cranfield 3-D model, using from 1 to 96 parallel processes 37

Figure 22: (a) Starting model guess, (b) final inversion result, and (c) estimated dimensionless parameter sensitivities of the 3-D inversion result of Section 3.4.4. 38

Figure 23: Data fits calculated from the preliminary 3-D inversion result of Section 3.4.4. 39

List of Tables

Table 1: Parameters and data misfit for the different flow and transport simulations. Model M0 is the starting point of the fully coupled inversion and models M1–M3 are the inversion results. Gray shaded cells mark active parameters and data sets in the different inversions; boldface marks the lowest misfit for each data set. Parameters are given with their estimated uncertainty (standard deviations).....31

Table 2: Arrival time of the CO_2 gas/supercritical phase at observation wells F2 and F3 31

Table 3: Data fitting errors calculated from the starting model (Iteration 0) and final model (Iteration 24) for each of the 7 individual data sets (see Commer et al., 2013).....37

Acronyms, Abbreviations, and Symbols

Term	Description
ρ	Resistivity
ϕ	Porosity
Φ	Objective function or misfit function
Ωm	Ohm-meter (SI unit of electrical resistivity)
1-D	One-dimensional
2-D	Two-dimensional
3-D	Three-dimensional
BiCGSTAB	Bi-conjugate gradient stabilized method
CASSM	Continuous active-source seismic monitoring
CH_4	Methane
CO_2	Carbon dioxide
DOE	U.S. Department of Energy
EC	Electrical conductivity
ER	Electrical resistance
ERT	Electrical resistance tomography
k	Permeability
LBNL	Lawrence Berkeley National Laboratory
mD	Millidarcy
MPa	Megapascal
m/s	Meters per second
NETL	National Energy Technology Laboratory
NRAP	National Risk Assessment Partnership
rms	Root mean square, also known as quadratic mean
S	Saturation
SECARB	Southeast Regional Carbon Sequestration Partnership
SF_6	Sulfer hexafluoride
SP	Self-potential
VSP	Vertical-seismic profiling

Acknowledgments

This work was completed as part of National Risk Assessment Partnership (NRAP) project. Support for this project came from the U.S. Department of Energy's (DOE) Office of Fossil Energy's Crosscutting Research program. This work was funded as part of the American Recovery and Reinvestment Act of 2009. The authors wish to acknowledge Traci Rodosta (Carbon Storage Technology Manager), Kanwal Majajan (Carbon Storage Division Director), M. Kylee Rice (Project Manager), Mark Ackiewicz (Division of CCS Research - Program Manager), Susan Maley and Steve Seachman (NETL Strategic Center for Coal), and Regis Conrad (DOE Office of Fossil Energy) for programmatic guidance, direction, and support.

The authors also wish to acknowledge the Cranfield and SECARB team for their scientific contributions and collaboration; Barry Freifeld and Paul Cook, Lawrence Berkeley National Laboratory (LBNL), for the U-tube design and many colleagues at the Texas Bureau of Economic Geology and Gulf Coast Carbon Center for U-tube data collection; Douglas LaBrecque (Multi-Phase Technologies, LLC) for assistance in acquiring the electrical resistance tomography (ERT) data; and David Freeman of Sandia Technologies for well design, instrumentation deployment and field site support. Denbury Onshore, LLC provided essential assistance to the project.

EXECUTIVE SUMMARY

This report is one of two deliverables resulting from a Lawrence Berkeley National Laboratory (LBNL) National Risk Assessment Partnership (NRAP) project that aimed at developing, testing, and applying novel methods for modeling geologic storage of carbon dioxide (CO_2) and jointly inverting monitoring data for leakage detection. This first NRAP report summarizes the method for jointly inverting hydrological and geophysical monitoring data. The ability to identify potential leakage pathways with monitoring data and continually monitor localized leakage of CO_2 and/or brine is essential for the science-based quantitative risk assessment at the core of the mission of NRAP. The second NRAP report describes the development, demonstration, and application of an inversion-based methodology for early leakage detection using pressure and surface deformation monitoring data.

Geophysical data hold great potential for improved characterization of subsurface properties and processes, but can be challenging to analyze because of resolution limitations and indirect or ambiguous relationships with hydrological properties. Prior work has shown that the usefulness of geophysical data can be improved when analyzed in a framework that jointly integrates geophysical and hydrological data while taking into account complex flow and transport processes.

The main goal of this work was to develop and test an approach for the coupled (joint) inversion of hydrological and geophysical data for improved prediction of CO_2 migration in the subsurface. The procedure resulted not only in an estimate of the CO_2 distribution in the subsurface, but also a calibrated hydrological model that can be used to better understand and predict CO_2 migration. While the particular methods used depend on characteristics of the site of interest and the types of measurements that were available, the inversion approach included the following main components:

1. A hydrological forward model that simulates flow and transport, such as that resulting from the injection of CO_2 and/or tracers, and also simulates the corresponding time-lapse hydrological measurements
2. A procedure for mapping the simulated hydrological properties and system state onto the geophysical numerical grid (the hydrological and geophysical numerical grids are usually different)
3. Petrophysical models that relate the hydrological state variables (e.g., CO_2 saturation, fluid density, temperature and pressure) to geophysical properties (e.g., elastic moduli or electrical resistivity)
4. Forward models that simulate the geophysical measurements at the corresponding survey times
5. An optimization algorithm that iteratively repeats steps (1) through (4), aiming to find estimates of the unknown parameters by minimizing the misfit between the measured and simulated hydrological and geophysical data

The approach is presented in Section 2, including a description of the coupled hydrological-geophysical inverse modeling framework that was implemented in iTOUGH2, details about the corresponding hydrological and geophysical forward modeling procedures, and a brief demonstration of how the new coupled modeling capabilities can be used to analyze seismic and hydrological data from the Frio II pilot test.

In Section 3, an in-depth case study is presented that evaluated how electrical resistance monitoring data, when used together with hydrological data in the coupled hydrological-geophysical framework, can help constrain models for simulating CO_2 migration at the Southeast Regional Carbon Sequestration Partnership (SECARB) pilot site located in Cranfield, Mississippi. Time-lapse electrical resistance tomography (ERT) data was analyzed first in an effort to identify a reliable form of the data to aid in calibrating flow and transport models in subsequent steps. While it was apparent that the resistivity increases due to the arriving gas phase CO_2, ERT inversions were strongly improved by including borehole log data as a structural constraint. Inversion of ERT data for two dimensional (2-D) and three-dimensional (3-D) resistivity distributions compared well with previously published results, though the estimated 3-D resistivity distributions showed out-of-plane (i.e., the plane formed between the observation wells) variations, indicating 3-D effects may be significant and should be considered in future research.

There may be insufficient information to image the fine-scale CO_2 movement through the reservoir due to data quality limitations. However, a reduced form of the ERT data, namely the time series of average resistivity calculated for the three main reservoir layers, showed a clear and consistent increase in resistivity during the experiment and was a robust form of the data to use for coupled hydrological-geophysical inversion. Inversions were performed with models of increasing complexity that used the reduced form of the ERT data along with the gas composition data. Models with different discretization and dimensionality were considered, including a radial model, a model combining three one-dimensional (1-D) layers, and a 3-D model with three layers of finely meshed 2-D grids. These increasingly complex models allow for different flow characteristics of the reservoir to be examined with manageable computational requirements. While inversion of gas composition data alone does not give reliable results for reservoir properties in a simplified reservoir model, the electrical resistance data improved the inversion due to a large measurement footprint and direct link to gas saturation. A more computationally intense, 3-D forward model, built on the basis of the inversion results obtained with 1-D layers, provided some confirmation of the parameter estimates since the electrical resistance, CO_2 gas mole fraction and tracer data were fit reasonably well. Preliminary inversion using an expanded 3-D model and newly implemented parallel computing capabilities showed that allowing for 3-D heterogeneity in each of the main geological layers substantially improved the fit to the data.

In general, these findings show potential benefits of monitoring CO_2 migration with geophysical data, as well as possible limitations due to poor data quality and resolution. One of the challenges of coupled hydrological-geophysical inversion is in correctly identifying and modeling all key parameters and physical processes controlling the different data sets. While integrating different types of data can result in an improved underlying model of the subsurface system, in practice it is often difficult to adequately fit all available data due to model errors. Other challenges arise from inadequate data coverage and high measurement noise at the great depths relevant to CO_2 sequestration sites, leading to non-uniqueness in parameter estimates. In addition, the inverse modeling approach requires many forward simulations that are computationally expensive, especially for 3-D models and subsurface systems involving potentially non-isothermal, multi-component, multi-phase flow and transport, necessitating the use of parallel computing. However, as is shown in this work, successful application of the approach can be achieved through careful analysis and integration of complementary hydrological and geophysical data

sets, and the use of initially simplified conceptual models, followed by models with increasing complexity and computational demand.

Further details of the material presented in this report were given by Doetsch et al. (2012a, 2012b, 2012c, 2013) and Commer et al. (2013).

1. INTRODUCTION

Geologic storage of carbon dioxide (CO_2) is a promising approach to offset anthropogenic carbon dioxide emissions into the atmosphere that contribute to climate change. Deep saline aquifers have been identified as key target formations for storage due to their large spatial extent and high potential volumes. For the safe and efficient operation of underground CO_2 storage, it is important to monitor the migration of the CO_2 (Benson et al., 2005). Monitoring subsurface CO_2 distribution can help to identify leakage through faults and abandoned wells, so that remedial measures can be taken before contamination of potable groundwater occurs. Knowledge of the spatial extent of injected CO_2 is also useful for assessing and updating pre-injection estimates of available storage volumes and refining models of subsurface flow properties.

Crosshole geophysical methods could play a key role in integrated monitoring programs for deep CO_2 injections and have recently been tested at a variety of pilot storage sites (e.g., Hovorka et al., 2006, 2011; Giese et al., 2009). Their advantage is the comparably high spatial resolution at the inter-well scale of tens of meters and the sensitivity to changes in bulk properties, such as supercritical-phase or gas saturation. Examples of successful geophysical monitoring of injected CO_2 include seismic tomography (e.g., Ajo-Franklin et al., 2013; Daley et al., 2008), continuous active-source seismic monitoring (CASSM) (Daley et al., 2011), and electrical resistance tomography (ERT) (Bergmann et al., 2012; Carrigan et al., 2013).

Crosswell electrical resistance monitoring for environmental applications in the shallow subsurface is a well-established technique (e.g., Daily and Ramirez, 1995; Ramirez et al., 1993; Slater et al., 2000) and, recently, fully automated systems for long-term monitoring have become available (e.g., Coscia et al., 2012). ERT monitoring of CO_2 migration can build upon this knowledge base while developing field systems that are better suited for the hostile down-hole environment present in deep storage wells. ERT is useful for monitoring of CO_2 due to the strong electrical resistivity contrast between highly conductive reservoir brine and practically non-conducting supercritical or gas-phase CO_2. Modeling studies have demonstrated the potential for ERT monitoring of CO_2 sequestration projects (e.g., al Hagrey, 2012; Christensen et al., 2006; Ramirez et al., 2003). Successful CO_2 field experiments with ERT monitoring have been reported from experiments in Nagaoka, Japan (Nakatsuka et al., 2010), Ketzin, Germany (Bergmann et al., 2012), and Cranfield, Mississippi, USA (Carrigan et al., 2013).

Incorporating geophysical data, such as seismic and electrical resistance data, into hydrological investigations holds great potential for improved characterization of subsurface properties and processes, thanks to the high spatial coverage of geophysical measurements and their sensitivity to hydrological processes. Despite the growing popularity of such methods in recent years for monitoring subsurface processes, such as CO_2 migration, it remains challenging to analyze geophysical data and to extract information that can be used quantitatively to inform hydrological models. For example, electrical resistance (ER) data are sensitive to the bulk properties of interest for monitoring CO_2, but the data suffer from inherent resolution limitations (e.g., Ellis and Oldenburg, 1994), which are amplified by the harsh environmental conditions (e.g., high temperatures and pressures) that are found in deep reservoirs and lead to high noise levels. Furthermore, ambiguities arise in interpreting geophysical data that are difficult to resolve without additional information: electrical resistance data are sensitive to both the chemical composition and saturation of pore fluids, in addition to lithological heterogeneity; and seismic data are sensitive to the saturation and distribution of pore fluids, as well as to pressure variations and lithological heterogeneity.

Resolution limitations can be partly overcome by constraining geophysical inversions with structural information from borehole logs or other geophysical data. For example, in traditional ERT, including interfaces separating zones with strong resistivity contrasts is one piece of *a priori* information that dramatically improves the resistivity estimate of each zone or its evolution over time (see Section 3.3.3). Jointly inverting seismic and ERT data with structural constraints may be more beneficial than analyzing each data set independently (see Section 3.3.2). The usefulness of geophysical data can be dramatically improved by systematically including hydrological data in the analysis. Conversely, since geophysical data are sensitive to changes in fluid distributions, they can be used to infer the underlying hydrological properties, such as the permeability and porosity, when analyzed in a framework that jointly integrates a variety of different data types simultaneously while accounting for complex flow and transport processes.

The main goal of this work was to develop and test an approach for the coupled (joint) inversion of hydrological and geophysical data, which integrates the geophysical information directly into hydrological parameter estimation for improved prediction of CO_2 migration in the subsurface. The approach is presented in Section 2. In Section 3, an in-depth case study is presented that evaluates how electrical resistance monitoring data, when used together with hydrological data in the coupled hydrological-geophysical framework, can help constrain models for simulating CO_2 migration at the SECARB pilot site located in Cranfield, Mississippi.

2. METHODS

The following subsections describe the coupled hydrological-geophysical inverse modeling framework and the corresponding forward modeling capabilities. Problem-specific details of the methodology, such as those related to simulation of particular measurements, parameterization of the inverse problem, and the petrophysical relationships linking hydrological properties to geophysical properties are described in the corresponding sections of the studies presented below. Note that this study focused on coupled hydrological-geophysical processes without considering geomechanical effects. Including geomechanical processes and corresponding measurements (e.g., tiltmeter data or surface deformation derived from InSAR data) in the procedure would be a logical extension of this research.

2.1 COUPLED HYDROLOGICAL-GEOPHYSICAL INVERSION FRAMEWORK

The main goal of this work was to develop and test an approach for the coupled (joint) inversion of hydrological and geophysical data for improved prediction of CO_2 migration in the subsurface. While the particular methods used depend on characteristics of the site of interest and the types of measurements that are available, the inversion approach includes these main components:

1. A hydrological forward model that simulates flow and transport, such as that resulting from the injection of CO_2 and/or tracers, and also simulates the corresponding time-lapse hydrological measurements
2. A procedure for mapping the simulated hydrological properties onto the geophysical numerical grid (the hydrological and geophysical numerical grids are often different, including the grid block sizes and the total extent of the model regions, depending on the requirements of the methods used)
3. Petrophysical models that relate the hydrological state variables (e.g., CO_2 saturation, fluid density, temperature and pressure) to geophysical properties (e.g., elastic moduli or electrical resistivity)
4. Forward models that simulate the geophysical measurements at the corresponding survey times
5. An optimization algorithm that iteratively repeats steps (1) through (4), aiming to find estimates of the unknown parameters by minimizing the misfit between the measured and simulated hydrological and geophysical data. This procedure results not only in an estimate of the CO_2 distribution in the subsurface, but also a calibrated hydrological model that can be used to better understand and predict CO_2 migration.

Building on previous work in which coupled hydrological-geophysical inverse modeling was performed for different applications (Kowalsky et al., 2004, 2005, 2008, 2011b), the approach was implemented in the inverse modeling framework iTOUGH2 (Finsterle, 1999a,b; 2004), which provided parameter estimation, parameter sensitivity, and uncertainty propagation capabilities to the general-purpose reservoir simulator TOUGH2 (Pruess et al., 1999) and which included capabilities for simulating geophysical measurements internally or by calling standalone executables. The mapping algorithm was based on a nearest neighbor interpolation that consisted of finding the TOUGH2 grid block that was closest to each geophysical grid block, resulting in a list of TOUGH2 grid blocks and their corresponding properties at a given time for the geophysical grid blocks. Since the geophysical grid was larger in some cases than the

TOUGH2 grid (see the second component of the inversion approach described in the previous paragraph), mapping exceptions were made for geophysical properties that were outside of the TOUGH2 model space (i.e., geophysical properties are assumed or inferred from site characterization data in those regions, and remain fixed during the simulation). Since petrophysical models depend on the methods being considered and site conditions, the user is enabled to specify the desired petrophysical models in iTOUGH2, whether for seismic properties (effective bulk and shear moduli) or electrical properties (effective resistivity). Various properties that are needed for the petrophysical models, such as the fluid densities, were calculated in TOUGH2 as a function of properties that vary during a simulation (e.g., pressure, temperature, salt mass fraction, and CO_2 saturation). In addition, geometrical parameters of the numerical grid (such as reservoir width, as described in Section 3.2.3), can be considered unknown parameters and estimated in the inversion through use of the PEST protocol (Doherty, 2008) in which certain aspects of the TOUGH2 mesh file are modified automatically during the inversion (Finsterle, 2010; Finsterle and Zhang, 2011). While a variety of optimization algorithms are available in iTOUGH2, the Levenberg-Marquardt method (Levenberg, 1944; Marquardt, 1963) was used in this study.

Aside from its usefulness in performing inverse modeling, the coupled modeling framework is also useful for evaluating the sensitivity of different geophysical measurements for monitoring hydrological processes. For example, the feasibility of monitoring production from gas hydrate reservoirs using vertical-seismic profiling (VSP) measurements was evaluated by Kowalsky et al. (2010). The framework could be used for experimental design, for example, to determine the optimal placement of measurements and the survey frequency, and to determine which data types are likely to be most sensitive to the relevant parameters for the application of interest.

2.2 HYDROLOGICAL FORWARD MODELING

Hydrological forward modeling refers to the simulation of the hydrological state variable (e.g., pressure, fluid saturation, salinity, and temperature) in an aquifer based on initial conditions, boundary conditions, sinks and sources, and based on hydrological model parameters, such as permeability or porosity. The simulation process involves the solution of mass and energy balance equations for fluid and heat flow. Hydrological forward modeling in this work was performed by TOUGH2, which solves the isothermal and non-isothermal multi-phase flow in multi-dimensional fractured-porous media (Pruess et al., 1999). The equation-of-state module ECO2N (Pruess, 2005) was used for simulations of the Frio II experiment described in Section 2.4 and module EOS7C (Oldenburg et al., 2004) was used for simulations of the Cranfield experiment in Section 3.

While Pruess et al. (1999) provides a comprehensive description of the TOUGH2 program structure and execution, a short summary is given here. TOUGH2 uses a spatial discretization with an integral form of the balance equations on an unstructured grid. The first part of the computational workload involves assembling the Jacobian matrix and residual vector that constitute the system of equations to be solved for each discrete time step, where time is discretized fully implicitly using first-order backward finite differences. The main computational load results from solving the equation system, given in residual form, for the time-dependent primary thermodynamic unknowns for each grid block, using the Newton-Raphson iteration method.

Some of the inversions presented in this report benefited by the use of MPiTOUGH2 (Commer et al., 2013), which uses parallel versions of the TOUGH simulators, referred to as TOUGH2-MP, that employ domain decomposition methods (Zhang et al., 2008) in order to distribute the workload of residual equation assembly and solution across multiple processes. While this study used spatial domain decomposition methods, algebraic decomposition of the arising system matrices is another option for the parallel forward modeling operator. TOUGH2-MP utilized the METIS partitioning algorithm developed by Karypsis and Kumar (1998) for the domain decomposition. Further, for the solution of the linear systems arising at each Newton-Raphson iteration step, the parallel iterative solver library AZTEC (Tuminaro et al., 1999) was used. Point-to-point message passing is needed to exchange properties between processes that share mesh elements at boundaries of the subdivided domain. While MPiTOUGH2 has preserved the choice of the original (direct and iterative) single-threaded TOUGH2 solvers (Moridis and Pruess, 1998), the BiCGSTAB (bi-conjugate gradient stabilized method) of the AZTEC library was used for parallel simulations. Additional message passing was internal to this solver.

Other recent developments in the TOUGH family of codes were described by Finsterle et al. (2013).

2.3 GEOPHYSICAL FORWARD MODELING

This study implemented the capability to simulate seismic travel times (straight- and curved-ray algorithms), directly measured ERT observations (resistance values), and a reduced form of ERT data, namely, the average electrical resistivity value (or relative changes thereof) in a specified region or layer to enable modeling of time-lapse geophysical data sets within iTOUGH2 in the context of CO_2 injection and storage. The average electrical resistivity is a reduced form of ERT data in which the average ERT value for a given region and survey time is calculated through geophysical tomography in a pre-processing step. As is discussed in Section 3.3.4, due to the high noise in the ERT data, this reduced form was found to be useful for the subsequent hydrological-geophysical inversions of Section 3.4. The code BERT (Günther et al., 2006) was used for all the ERT inversions of Section 3.3 except for those of Section 3.3.5 in which the geophysical modeling and imaging package EMGeo (e.g., Commer et al., 2011) was used. The code PSTOMO (Tryggvason, 2009) was used for curved-ray seismic travel time calculations in the short demonstration of Section 2.4.

2.4 DEMONSTRATION FOR SEISMIC AND HYDROLOGICAL MEASUREMENTS

A model was developed which simulates the injection of CO_2 into a brine aquifer (Figure 1) to demonstrate the hydrological-geophysical modeling concept. After the onset of CO_2 injection, hydrological measurements (pressure and saturation in two wells) and geophysical measurements (crosshole seismic travel times for a fixed source and receiver) were simulated based on two monitoring wells that were spaced 10 m apart. A coupled hydrological-geophysical simulation resulted in simulated hydrogeological-geophysical data that showed sensitivity to changes in the reservoir caused by the injection of CO_2 (Figure 3). It is interesting, though not surprising, to note that the sensitivity of the seismic travel time to the CO_2 front critically depends on the petrophysical model.

A coupled hydrological-geophysical model (Figure 3) was also developed for simulating a small-scale Frio II pilot experiment in which supercritical CO_2 was injected into a brine formation while hydrological and seismic measurements were performed (Kowalsky et al., 2011a). More

specifically, CASSM data were collected in a crosswell configuration using a fixed source and sensors, allowing for the continuous monitoring of seismic waveforms at a high temporal sampling rate (Daley et al., 2008). In addition to the CASSM data, CO_2 saturation in an observation well was measured. Compared to a previous study in which the experiment and measurements were modeled in a loosely coupled fashion (Daley et al., 2011), this study found that an improved match between the measured and simulated observations could be obtained when the models were fully coupled, and this resulted in a refined understanding of heterogeneity and CO_2 migration at the site.

Results in this section were intended to demonstrate the seismic capabilities. The final analysis of the Frio II coupled modeling study is still ongoing.

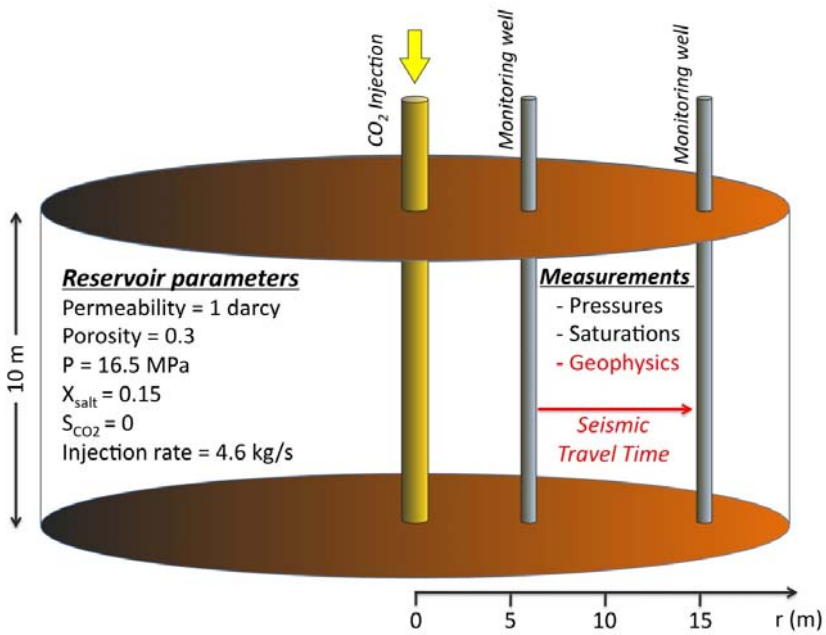

Figure 1: Schematic of the problem used to demonstrate coupled hydrological-geophysical modeling. This model is a modified version of sample problem rcc3 from Pruess (2005), which simulated the injection of CO_2 into a brine aquifer. A CO_2 injection well fully penetrated a homogeneous, isotropic, infinite-acting aquifer of 10 m thickness. Hydrological measurements (pressure and saturation) and geophysical measurements (crosshole seismic) were simulated based on two observation wells 5 and 15 m from the injection well, respectively.

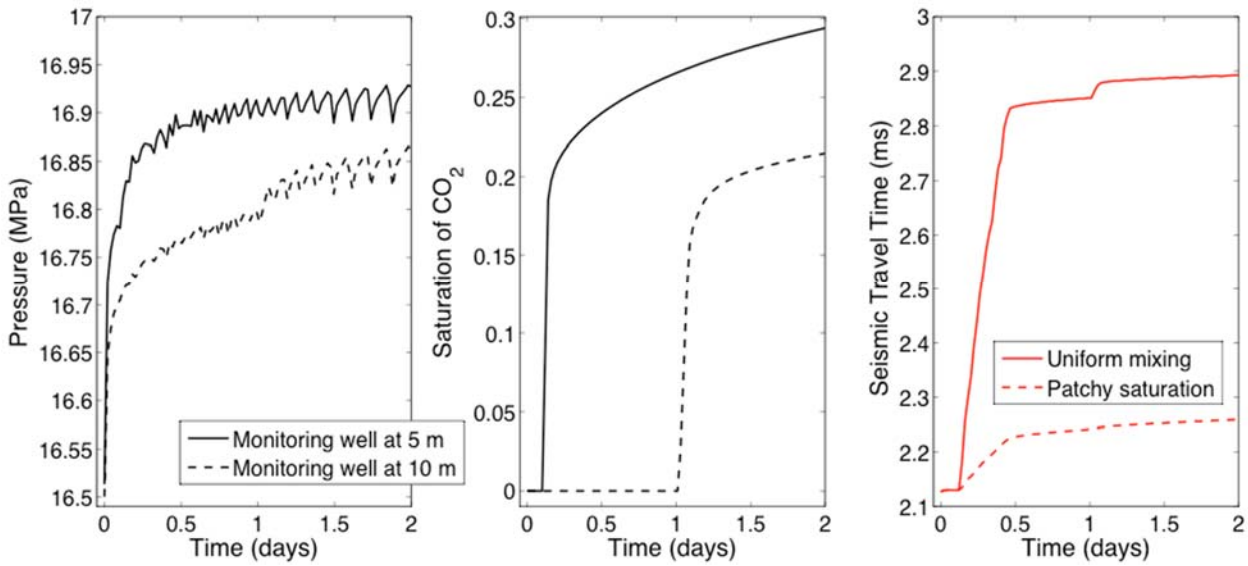

Figure 2: Example of measurements that can be modeled in a coupled hydrological-geophysical simulation. The simulated pressures (left) and saturations (middle) at two observation wells and the crosshole seismic travel times (right) are shown as a function of elapsed time since the start of the CO_2 injection. The seismic response (right) is shown for two cases in which the Gassmann equation was used to calculate the effective velocity with the bulk modulus of the CO_2-brine mixture calculated assuming a homogenous distribution (Reuss average, solid line) and a patchy distribution (Voigt average, dashed line).

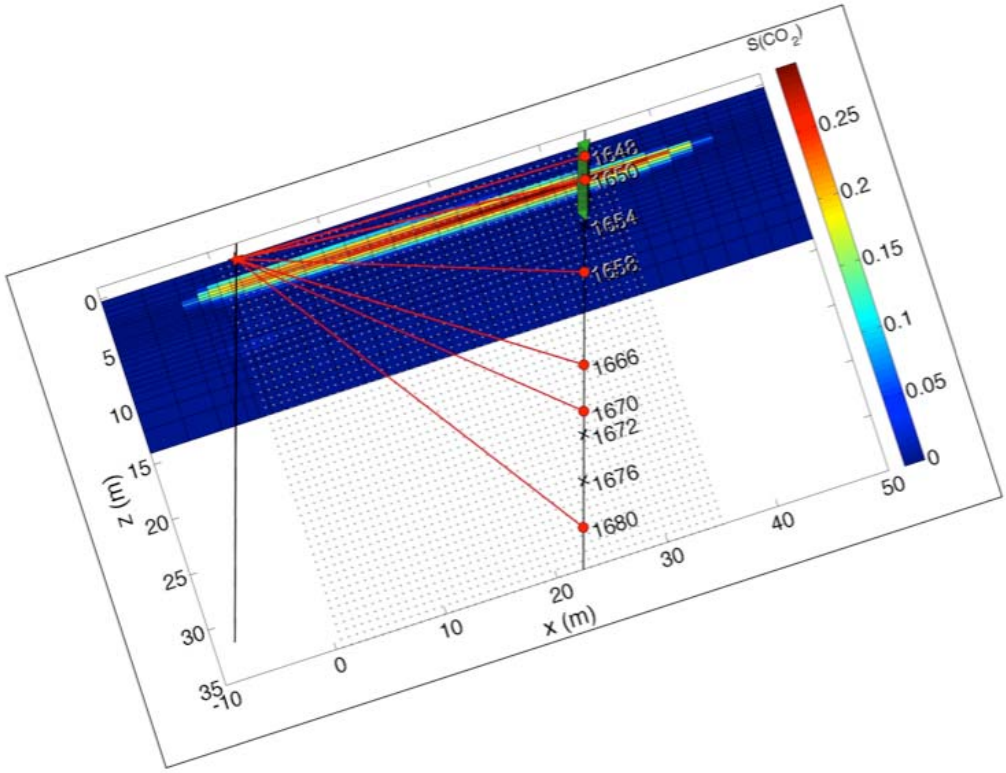

Figure 3: 2-D hydrological model for Frio II experiment with overlapping geophysical grid for simulating seismic travel times. The right and left boundaries of the hydrological model are outside of the pictured region.

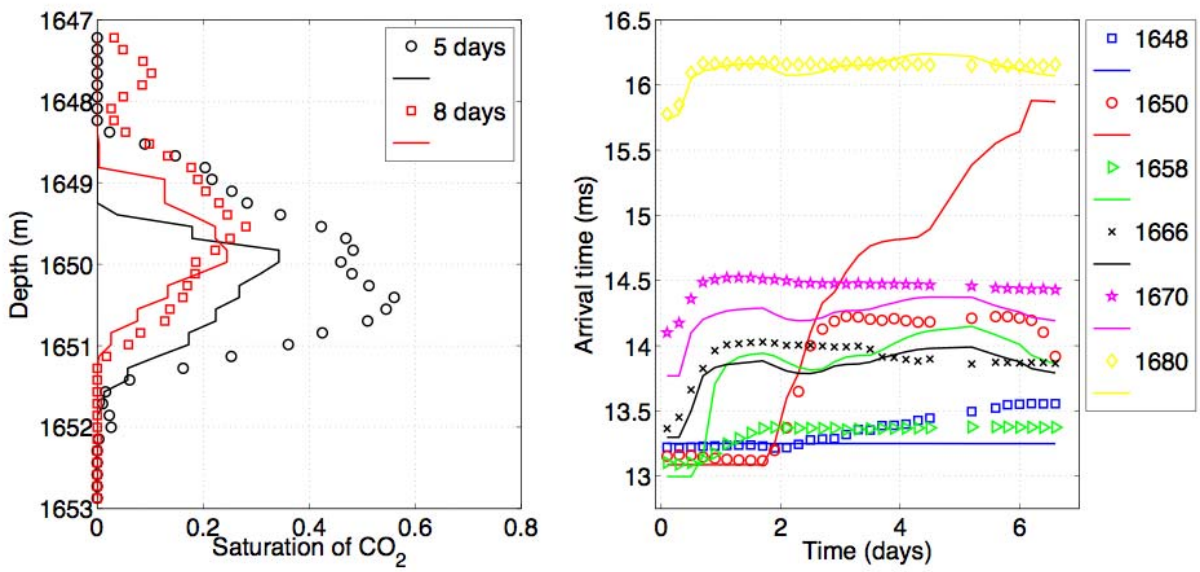

Figure 4: Example of simulated (solid lines) and measured (symbols) CO_2 saturation (left side) and seismic travel times (right side).

3. CRANFIELD STUDY

The goal of this study was to evaluate how time-lapse ERT data, when combined with hydrological data in a coupled hydrological-geophysical modeling framework, can help constrain simulations of CO_2 migration for the SECARB pilot site located in Cranfield, Mississippi. After describing the field site, injection experiment, and various data sets that were collected (Section 3.1), and providing some details on the inversion components (Section 3.2), time-lapse ERT data with structurally unconstrained and constrained ERT inversions (Section 3.3) was analyzed in an effort to identify a reliable form of the data that can help calibrate flow and transport models. ERT-derived changes in subsurface electrical resistivity was used along with gas composition data for hydrological-geophysical inversion (Section 3.4), followed by a discussion and conclusions from the Cranfield study in Sections 3.5 and 3.6, respectively.

3.1 FIELD SITE AND CO_2 INJECTION EXPERIMENT

3.1.1 SECARB Cranfield Pilot Site

The SECARB Cranfield pilot site (~20 km east of Natchez, Mississippi) was chosen for a large scale (1 M tonne) CO_2 injection into a brine-filled reservoir at ~3,200-m depth. The injection interval is a segment of the Lower Tuscaloosa Formation referred to as the Tuscaloosa D/E sand. This unit consists of relatively permeable fluvial sandstones and conglomerates. The system is described as having fluvial point-bar and channel deposits by Lu et al. (2012b), who found that mineral reactions during CO_2 injection were minor over short time periods (months) and brine chemistry remained largely unchanged. The salinity of the reservoir brine is ~155,000 mg/L.

The target formation was accessed by one injection well (F1) and two observation wells (F2 and F3). Around the injection well, the Tuscaloosa D/E formation dips 2 degrees toward the east, and the two observation wells are located down-dip at distances of ~70 m and ~100 m (see Figure 5). The ground surface at F2 (96 m above mean sea level) was used throughout this study as depth reference, as was done in Ajo-Franklin et al. (2013).

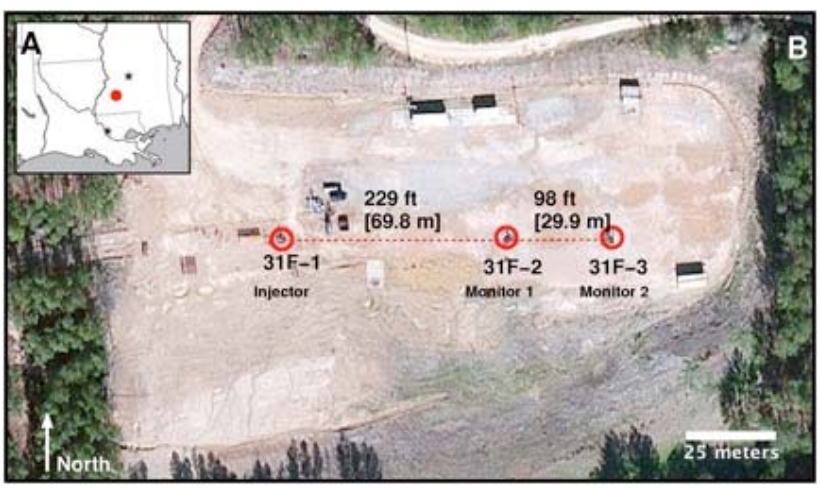

Figure 5: (a) Location of the Cranfield site (red dot) in Mississippi. (b) Photograph of site showing injection borehole 31F-1 (F1) and observation boreholes 31F-2 (F2) and 31F-3 (F3) (Ajo-Franklin et al., 2013).

3.1.2 Borehole Logging Data

Pre-injection characterization of the site included geophysical borehole logging as well as whole core and sidewall samples (see Butsch et al., 2013). Downhole spontaneous-potential (SP) data (Figure 6a) clearly show the depth interval of the Tuscaloosa formation, which confirms the 2% dip toward the east as well as the reservoir thickness of approximately 24 m (depth of 3,176–3,200 m at well F2). The SP logs also indicated an interruption of the Tuscaloosa sands at depth 3,192 m. Lu et al. (2012b) identified this thin layer as a calcite-rich shale baffle, which has much lower porosity and is much tighter than the Tuscaloosa sands. The shale baffle is thus unlikely to support considerable flow and transport and possibly separates the reservoir into two largely unconnected layers although continuity of the feature outside of the plane formed by the three wells considered in this study is difficult to verify.

The mean of the porosities derived from sonic logs and those derived from neutron-neutron logs were used to get porosity-depth functions for each of the three wells. The depth axis of the F1 and F3 logs were then shifted to account for the 2 degree formation dip (Figure 6c) and a unique porosity-depth function was derived by taking the median of the porosities for the three wells at each depth. Based on this porosity function (gray line in Figure 6d), the reservoir was divided into three depth sections (black line in Figure 6d): the two bottom sections with porosities greater than 20% and the third one at the top with porosities on average below 20%. The average porosities for those layers—from top to bottom—are 19.6%, 23.9% and 22.9%. Porosity variations within each layer are ~3%, but uncertainty from different averaging techniques are only ~0.2%. The average layer porosities were used to populate the meshes for the CO_2 migration simulations described in subsequent sections.

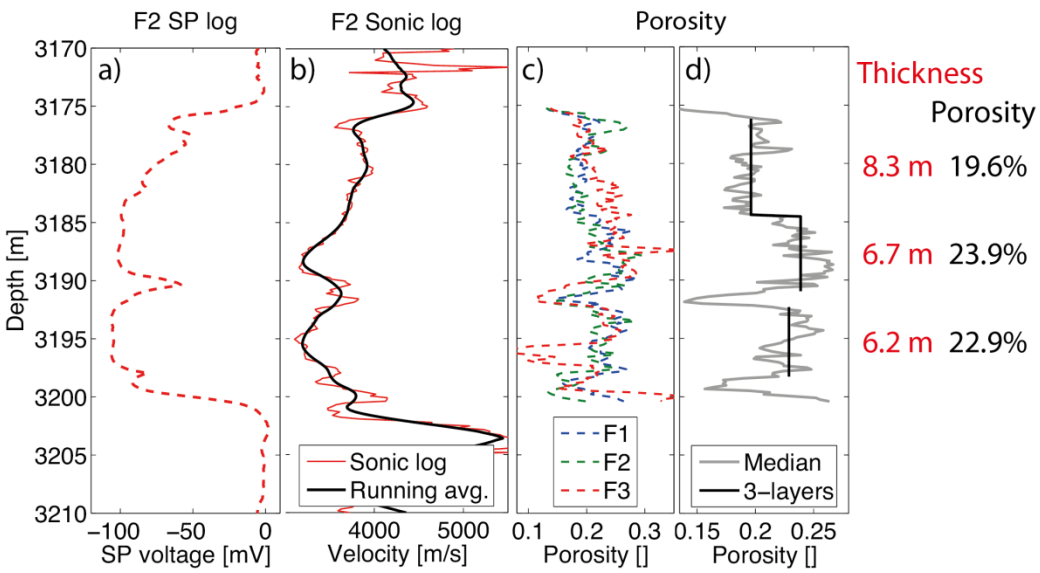

Figure 6: Select geophysical borehole logging data. (a) Self-potential (SP) and (b) sonic log in borehole F2. (c) Porosity based on sonic and neutron–neutron data in the three boreholes (depths are dip-corrected to F2 depth) and (d) median porosity of the three boreholes and averages for a 3-layer model. Layer thicknesses and porosities for a division into three layers are shown to the right.

3.1.3 CO_2 Injection and Hydrological Monitoring Data

CO_2 injection in borehole F1 was initiated on December 1, 2009 and all subsequent time references are relative to that date. The initial injection rate was 3 kg/s, which was increased to 5.7 kg/s on day 18 (December 18) and stayed stable until day 30, which marks the end of the main period of interest here. It is assumed that the injected fluid contained 98–99% CO_2 and 1–2% CH_4 (methane). On day 3, 40 kg of sulfur hexafluoride (SF_6) tracer was co-injected with the CO_2 and CH_4 over a period of a few minutes. With reservoir temperatures and pressures around 126°C and 31.9 MPa (319 bar, 4627 psi), respectively, the CO_2 and CH_4 existed as a mixed phase in supercritical form. Throughout the description of this study, the term gas and gas saturation is used to describe this supercritical CO_2 and CH_4 phase and its saturation.

The key part of the hydrological monitoring consisted of continuous gas composition analysis. The gas phase was collected using a U-tube sampler (Freifeld et al., 2005; Lu et al., 2012a), with one sampler in each of the two observation wells F2 and F3. The samples were analyzed in real time using an onsite mass spectrometer (Doughty and Freifeld, 2013; Lu et al., 2012a). The U-tube system allowed continuous measurement, and samples were analyzed 1–3 times per hour. The borehole perforation or the U-tube intake was initially clogged so that no measurements could be taken at first, but the arriving CO_2 apparently lubricated the system and allowed high-quality measurements thereafter. The initial arrival of the gas phase was thus not fully captured by the sampling system. The clogging and CO_2 lubrication occurred in both observation boreholes (F2 and F3).

The mole fractions in the gas phase measured in F2 and F3 are shown in Figure 7. The first observation in Figure 7a is that the methane concentration is falling at the beginning of the time series, which implies that the methane concentration was higher at earlier times and actually arrived before the CO_2. This can be explained by dissolved methane being swept out of the liquid phase due to co-solubility limitations, when the injected CO_2 starts to dissolve (Doughty and Freifeld, 2013). In this case, the reservoir brine must be close to full methane saturation prior to injection. High methane concentrations during the pre-injection period are likely due to the reservoir being in the water leg of an anticlinal hydrocarbon reservoir. Possibly, some free-phase methane even existed in the reservoir prior to injection. In either case, a small methane gas phase traveled ahead of the injected CO_2. The effect of a leading methane gas phase is confirmed by flow and transport simulations (see Doughty and Freifeld, 2013 and Section 3.4).

Figure 7a also shows two distinct CO_2 and CH_4 arrivals in each well. The contributions to these time series were interpreted as coming from different flow paths, probably two unconnected depth sections (e.g., two layers separated by an impermeable shale baffle, as described above). The methane gas phase appears to arrive first through each of these flow paths, but the peak of the first arrival is missing in the data due to the clogged U-tube system. The first methane arrival is followed by the arrival of the CO_2 through the same flow path at days 11 and 15 in F2 and F3, respectively. The CO_2 gas mole fraction then decreases as the methane arrives through the second flow path and increases for the remainder of the time series as the CO_2 also arrives through this second flow path at days 14 and 17 in F2 and F3, respectively. The SF_6 tracer in Figure 7b shows the same double arrival, with the first arrival being only partly measured due to the initial U-tube problems.

The complicated gas-phase arrivals and the interplay between methane and CO_2 illustrate the complexity of the mechanisms that need to be considered. These complexities, especially the

critical role of methane, have strong implications for flow and transport simulations that need to include brine, CO_2, methane and tracer in the liquid and gas phases, with precise accounting of phase-partitioning effects.

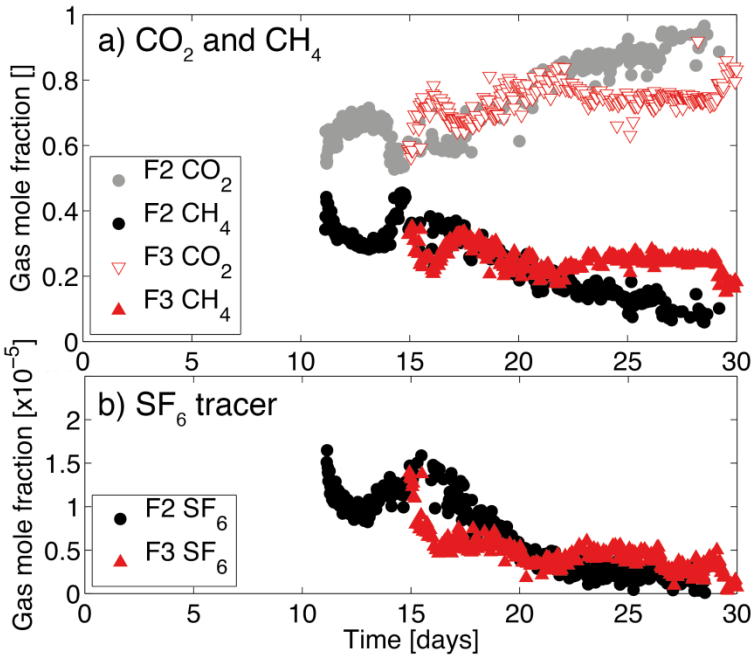

Figure 7: Gas composition monitoring data measured with a U-tube device in observation wells F2 and F3. (a) Mole fraction of CO_2 and CH_4 and (b) SF_6 tracer injected with the CO_2 on day 3. Early time data is missing because the U-tube device was initially clogged; it was apparently freed by the arriving CO_2.

3.1.4 Geophysical Monitoring Data

The geophysical monitoring planned for the Cranfield site included continuous active source seismic monitoring (CASSM, Daley et al., 2007) and ER surveys. In addition, cross-well seismic tomography data were recorded prior to injection and after over 9 months of injection (Ajo-Franklin et al., 2013). Unfortunately, the CASSM receiver system failed after about one month of operation, just before the injection of CO_2 started, and could not be repaired.

While the goal was to test an approach for coupled inversion of hydrologic and geophysical monitoring data in the context of CO_2 monitoring, it was necessary to gain a good understanding of the collected geophysical data to learn about its quality and sensitivity to subsurface properties at the site. Therefore, significant efforts were made in processing and analyzing the seismic and ERT data.

Collection and Analysis of Crosswell Seismic Tomography Data

Crosswell seismic data were acquired between F1–F2–F3 before the start of the CO_2 injection and a second data set between F2 and F3 was acquired after ~300 days of CO_2 injection. Doetsch et al. (2012a) and Ajo-Franklin et al. (2013) found that between observation wells F2 and F3, the

gaseous CO_2 was mostly concentrated in two layers in the lower part of the reservoir. These two zones correspond to the two high-porosity intervals shown in Figure 6d.

Described in the remainder of this subsection are results presented by Doetsch et al. (2012a). The baseline data were inverted using an Occam's type inversion with an assumed travel time error of 1.5% and travel times in the 7–21 meters per second (m/s) range. A homogeneous 4,000 m// starting and reference model was used with a stochastic regularization and integral scales of 4 and 10 m in vertical and horizontal direction, respectively. The baseline seismic tomograms revealed nice structure (Figure 8a), with the saline aquifer characterized by low velocities, and with good agreement with the sonic logs (Figure 8b). The Lower Tuscaloosa formation can be identified by the low velocities between depths of 3,180 and 3,205 m.

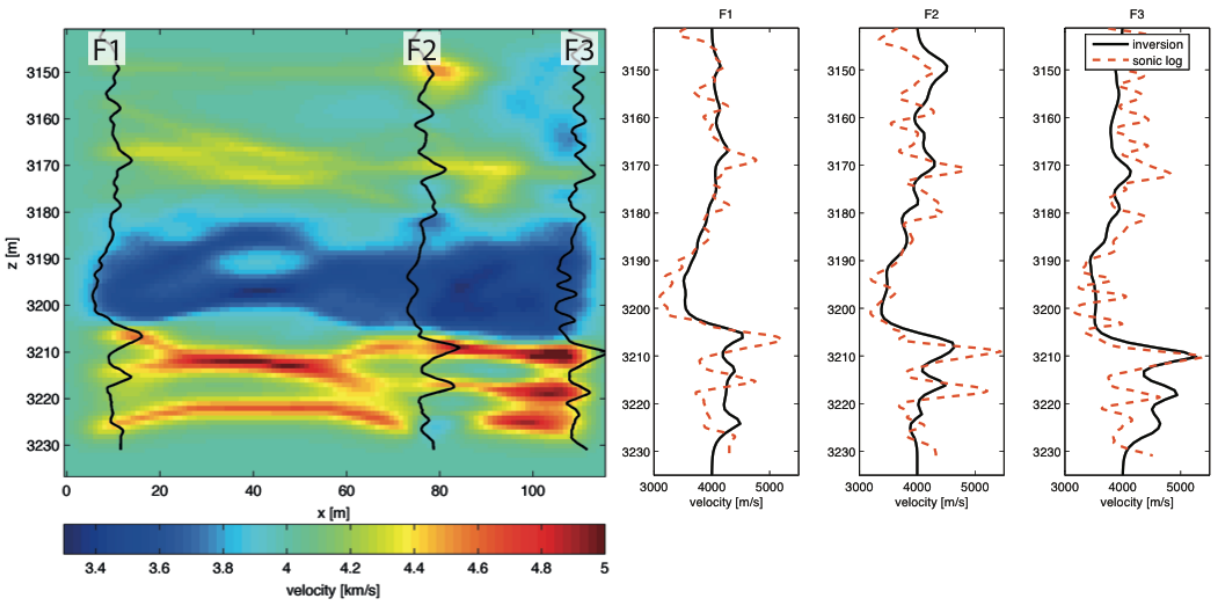

Figure 8: Seismic velocity distribution from inversion of baseline (pre-injection) crosswell data (left side), and comparison of inversion with (smoothed) sonic logs at the three observation wells (right side).

The second data set collected between F2 and F3 was used to invert for CO_2 induced changes in velocity, using the baseline result as the start and reference model, resulting in the changes shown in Figure 9a. Other types of inversion of the seismic data were performed, including a single parameter inversion, which revealed a decrease in seismic velocity in the region of the CO_2 plume of around 215 m/s (Figure 9b). Joint inversion of the seismic and ERT data at a late survey time was also performed (see Section 3.3.2), resulting in a more focused CO_2 plume than in individual inversions.

Since the seismic data were only collected before and again long after the start of injection, they were ultimately not included in coupled hydrological-geophysical inversions.

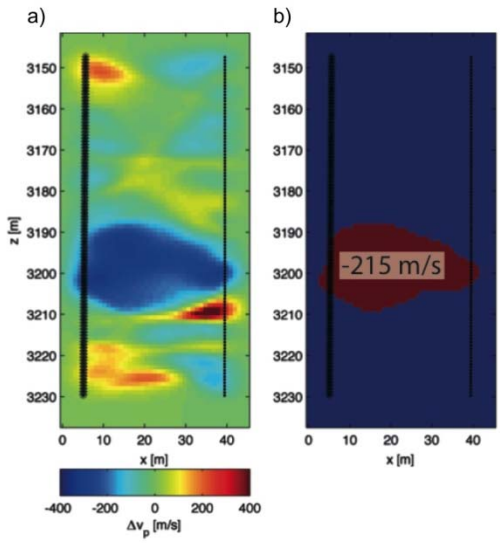

Figure 9: Inversion for CO_2-induced-changes in seismic velocity, from baseline to after nearly 10 months of injection, (a) using stochastic regularization to estimate a change in velocity at each point and (b) estimating only a single value for the change in velocity within the plume region (where the plume region is defined as the pixels within (a) within which the velocity decreases by more than 160 m/s).

Collection of Electrical Data

The ERT monitoring system was installed with electrodes in wells F2 and F3. Carrigan et al. (2009, 2013) designed an ERT acquisition system for the specific conditions and monitoring target at Cranfield. The high temperature of 126°C and pressure of 31.9 MPa, and the low pH of 3 required special design and installation. A total of 21 stainless steel electrodes were mounted outside the fiberglass casing, with 14 electrodes at 4.5 m spacing in borehole F2 and 7 electrodes at a 9.0 m vertical spacing in F3. Insulated and armored cables ran from each electrode to a fully automated and remotely controlled acquisition system at the surface (Carrigan et al., 2009, 2013).

ERT monitoring was initiated on November 25, 2009, 5 days before the start of the CO_2 injection. The computer controlled acquisition system recorded data continuously, following a four-electrode measurement scheme with current and potential electrodes sweeping through both boreholes (Carrigan et al., 2013). Full reciprocal measurements (switching current and potential electrodes) were included in the measurement sequence for noise estimation. ERT monitoring continued for ~300 days (until September 2010), with ~7,000 measurements acquired per day.

Pre-processing of Electrical Data

Initial quality control and data analysis indicated that the general noise level was high, with many measurements showing unrealistic resistance values. The long cables, deployed outside of casing, and the unfavorable conditions at depth are suspected to be the main reasons for the strong signal disturbances. However, thanks to the high temporal acquisition rate and large number (~1,300) of measurement configurations, detailed analysis and filtering of the raw data allowed for useful information to be extracted, as is described next.

Time series of resistances for each measurement configuration were assembled to assess data quality. From these time series, a baseline resistance reading of the undisturbed brine-filled reservoir was extracted by averaging data from ±5 days of the beginning of the CO_2 injection. The baseline apparent resistivity $\rho_a(0)$ was then calculated for each measurement configuration by multiplying the resistance with the geometric K factor, which depends on the relative distances between the electrodes (see, e.g., Günther, 2004, p. 45). The apparent resistivity corresponds to the resistivity of a homogeneous earth that would yield the same measurement value and should thus not be far outside the expected subsurface resistivity range, assuming moderate resistivity contrasts within the reservoir. This possible range was defined as 0.001 Ωm < $\rho_a(0)$ < 100 Ωm, with the expected reservoir resistivity between 1 Ωm and 10 Ωm. All configurations outside this 0.001–100 Ωm range were excluded from further processing.

All time series were then down-sampled by averaging the data within 2-day time windows and normalized by the baseline apparent resistivity. Additional filtering concentrated on these relative $\rho_a(t)/\rho_a(0)$ variations with time t for each measurement configuration. Visual inspection of the time series showed that relative variation of all smoothly varying time series did not exceed a factor of 2, so all time series with values outside the range of $0.5 < \rho_a(t)/\rho_a(0) < 2$ were excluded. While this range might seem narrow, inversion tests with a wider $\rho_a(t)/\rho_a(0)$ cut-off range gave poorer results and the additional data needed to be down weighted in order to fit the data to the assumed error level.

While comparing resistances of reciprocal measurements is often performed to estimate the error level of individual measurements (e.g., Slater et al., 2000) and to exclude poor data, this study found that for this specific data set, corrupted data had to be removed first. Taking the average of reciprocal measurements and judging the data error on the basis of the difference between reciprocal data often compromised the high-quality data. Instead, outliers were first removed, using the criteria discussed above. The reciprocal measurements were then matched wherever they existed and the average of the two measurements was used for further processing. The reciprocal errors were added to a baseline error of 5% and the standard deviation of variations during the baseline averaging. These error estimates, with a median of 11.4%, were used in the ERT inversions.

The preprocessed $\rho_a(t)/\rho_a(0)$ time series in Figure 10 show a coherent picture of increasing apparent resistivities with time. Most time series were stable with little change around the baseline value for the first 15 days. Apparent resistivities then increased strongly for about 10 days, indicating an increasing resistivity within the reservoir due to increased gas saturation. After day 25, apparent resistivities were mostly stable, but continued to rise slightly. These normalized apparent resistivities can give a qualitative impression of the development of reservoir resistivity over time, but only ERT inversions can quantify these resistivity changes. Integrated analysis incorporating flow and transport modeling can further link the electrical data with the hydrological properties.

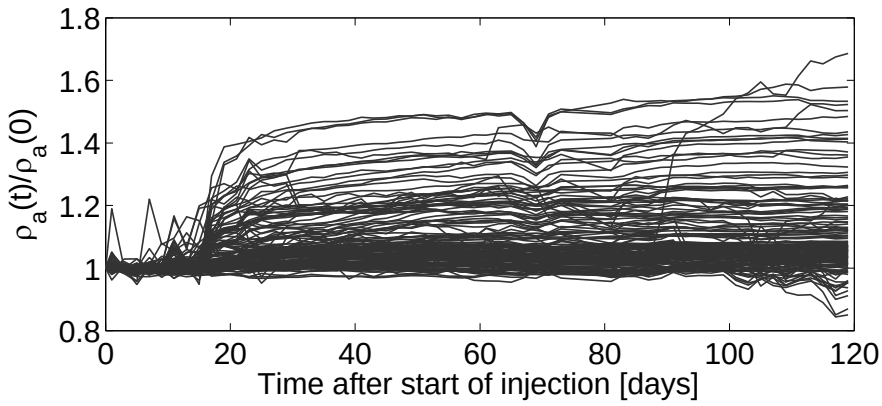

Figure 10: Time series of electrical resistance measurements using various electrode combinations in wells F2 and F3, normalized by the pre-injection resistances. The increase in measured resistances indicates a developing CO_2 and CH_4 gas phase between the measurement boreholes F2 and F3.

3.2 INVERSION COMPONENTS

3.2.1 Flow and Transport Simulations

As described in Section 2.2, for the flow and transport simulations, this study used the general-purpose numerical simulator TOUGH2 (Pruess et al., 1999) that included capabilities for modeling non-isothermal multi-phase, multi-component fluid flow in porous and fractured media. It used flexible finite-volume meshes with a multi-phase extension of Darcy's law, which included relative permeability and capillary pressure effects. The current case study utilized the TOUGH2 equation-of-state module EOS7C (Oldenburg et al., 2004) for multi-component gas mixtures in methane–carbon dioxide (CH_4–CO_2) systems, with or without an aqueous phase. EOS7C included an accurate solubility formulation to model flow and transport of gas and aqueous phase mixtures over a wide range of pressures and temperatures, including those in deep high-temperature reservoirs considered for CO_2 sequestration. The supercritical CO_2 was modeled as a non-condensible gas. EOS7C modeled the five components: water, brine, CO_2, methane, and a tracer. Each of these components was partitioned into an aqueous and a gas/supercritical phase according to the local thermodynamic conditions. All components were used, including the brine properties measured at the field site (salinity of ~155,000 mg/L). The reservoir brine was initially methane-saturated with no methane gas phase existing. , This study assumed non-isothermal effects were negligible for the modeling, and neglected molecular diffusion, which was not significant on the relatively short time scale of 30 days that was considered.

The model development (Section 3.4) in this study aimed to capture the key features of the system with models that are computationally efficient and only as complex as is warranted. Therefore, alternative conceptual models were built based on the supporting geological information and these models were calibrated by comparing the hydrological measurements (e.g., CO_2 mole fraction in the gas phase) directly with the modeling output. All models considered here were composed of three layers, based on the borehole-log porosity shown in Figure 6. These meshes differ in the discretization of the horizontal plane, while the cell sizes in the main lateral coordinate (radius or x, depending on the model) were the same for all meshes.

The meshes were finely discretized around the injection borehole, correctly implementing the borehole radius of 11 cm. Lateral grid size increased with distance from the injection well, to a cell width of 1 m that was used for all cells between the observation wells F2 and F3. Cell size increases further beyond F3, giving a total of 188 cells covering the 1,000 m total grid extent. No-flow boundary conditions were applied at the top and bottom of the reservoir and a constant pressure was maintained at the maximum radius or lateral distance. Modeling tests showed that the 2 degree geological formation dip does not influence the flow and transport simulations and it is thus neglected. The thin but tight shale baffle layer around depth 3,192 m (Figure 6) was included in the model as a thin aquitard by not allowing vertical flow between the two lower layers. However, vertical flow was permitted between the two top layers. CO_2 was injected into a single borehole cell connected to the two lower model layers, allowing for CO_2 partitioning into each layer according to the relative injectivity of each layer. While the three wells penetrate all layers, no vertical flow was allowed in the observation wells.

Models with different lateral discretizations that represent different dimensionalities were considered. As described in Section 3.4, a radial model was considered first, followed by a model combining three 1-D layers and finally a 3-D model with three layers of finely meshed 2-D grids. The different meshes not only represent different complexities, but they also help to understand the flow characteristics of the reservoir. For example, the reservoir volume that can be reached within a certain distance from the injection well in a radial flow system was much larger than in narrow flow channels represented by 1-D models. This relates directly to the long-term operation of a CO_2 injection facility, for example, because the amount of CO_2 that can be stored underground depends on the volume of accessible pore space.

3.2.2 Inversion of Time-Lapse ERT Data for use in Coupled Inversion

For ERT data to be incorporated in the fully coupled inversion, one can either (1) invert the ERT data first to produce spatial distributions of changes in subsurface resistivity at various times or (2) directly include the ERT data in the coupled inversion. In both cases, the subsurface resistivity needs to be linked to gas saturation through a petrophysical function. While the second option is generally preferred (Commer et al., 2012), the first option was chosen due to data quality limitations.

The time-lapse processing approach was based on the ratio inversion scheme introduced by Daily and Owen (1991). The input data to the inversion was the time-series of normalized apparent resistivities $\rho_a(t)/\rho_a(0)$, discussed in Section 3.1.4 and shown in Figure 10. Normalizing the input apparent resistivities with their pre-injection values removes the static error contributions that are a combination of modeling errors and systematic measurement errors due to ground coupling problems or geometrical errors. In cross-borehole ERT monitoring with permanent installations, these static errors are typically much larger than the time-varying errors of each time-lapse data set (e.g., Doetsch et al., 2010).

The inversion of the normalized apparent resistivities started with a homogeneous half space of 1 Ωm resistivity. The models that resulted from the ratio inversions show the spatial distribution of relative changes in electrical resistivity of the subsurface at a given time. Model values above 1 Ωm indicate an increase in resistivity; values below 1 Ωm indicate a decrease.

For a hydrogeological interpretation and comparison with the CO_2 migration simulation, these changes in resistivity were translated into aqueous saturation using Archie's law (Archie, 1942),

$$\rho = \rho_w \phi^{-m} S_w^{-n} , \tag{1}$$

which relates bulk resistivity ρ with the resistivity of the water (brine) ρ_w, porosity ϕ, aqueous saturation S_w and the empirical exponents m and n. The assumption behind Archie's law is that all electric current flows through the aqueous phase. The grains, their surfaces and the gas phase are thus modeled as non-conductive. This assumption is reasonable for this field site, where the brine resistivity is very low (~1 Ωm) and the target formation consists of sandstone that is not expected to support considerable surface conductance. Laboratory measurements on Berea Sandstone cores have also demonstrated the validity of Archie's law in brine (1 Ωm) – CO_2 systems (Onishi et al., 2006). While other sources can be excluded, it is possible that surface conductivity is supported by the relatively high surface area due to a high chlorite fraction in the Tuscaloosa D/E formation (Landrot et al., 2012). Electrical measurements on cores from Cranfield would be an interesting subject for future research.

When solving Equation1 for saturation S_w, the uncertainty is high, due to uncertainties in the other parameters. In the case of a resistivity time series $\rho(t)$ from time-lapse inversion, Equation 1 can be simplified to

$$\frac{\rho(t)}{\rho(0)} = \frac{1}{S_w(t)^n} = \frac{1}{(1 - S_{sc}(t))^n} , \tag{2}$$

with gas saturation $S_{sc}(t)$ and assuming an initial water saturation of $S_w(0)=1$, which is assumed to be valid for the experiment considered here. Equation 2 also assumes that ρ_w does not change with time. Although dissolving CO_2 has been shown to decrease the water resistivity (e.g., Dafflon et al., 2013), no significant effect is expected at the reservoir conditions of this field site. Given these assumptions, the only uncertainty in the petrophysical relationship is in the saturation exponent n, which in consolidated sands is commonly reported to be close to 2 (e.g., Archie, 1942). Uncertainty of 10% in n would result in uncertainty of 10% in the estimated saturation.

3.2.3 Parameterization and Optimization Details

The simulation of flow and transport and of the corresponding gas composition data (Section 3.1.3) and ERT-derived electrical resistivities were realized in the inversion framework iTOUGH2 (Finsterle, 1999b). The ERT-derived electrical resistivities were incorporated through the petrophysical function in Equation 2. iTOUGH2 allows estimation of unknown hydrological parameters, which can be groups of cells (e.g., layers) in the TOUGH2 mesh or distributed parameter fields (e.g., Kowalsky et al., 2005). In addition, geometrical parameters, such as reservoir width, can be considered unknown parameters that are estimated in the inversion through use of the PEST protocol (Finsterle, 2010; Finsterle and Zhang, 2011) in which certain aspects of the TOUGH2 mesh file are modified automatically during the inversion.

In the inversions discussed here, the parameters of interest are reservoir permeability and effective reservoir width. As mentioned above, three-layer models were used with the main parameters being horizontal and vertical permeability in these layers. Layer-wise parameterization was chosen over fully distributed parameter fields to avoid over-parameterization and the associated increased parameter uncertainty. An additional parameter of

interest was the effective reservoir width, which represents the lateral width accessible to the injected CO_2. This effective width was related to the size of the flow channels in the fluvial deposits of the reservoir. In the coupled inversion, the Levenberg–Marquardt minimization algorithm was used to optimize the objective function

$$\Phi = \Phi_{res} + \Phi_{gc}, \tag{3}$$

where Φ_{res} and Φ_{gc} are the resistivity and gas composition misfit functions. The Φ_{res} value is given by

$$\Phi_{res} = \sum_{\min(t)}^{\max(t)} \sum_{i} \left(\frac{d_i(t) - s_i(t)}{\varepsilon} \right)^2, \tag{4}$$

with the measured data $d_i(t)$ at time t, its simulated equivalent $s_i(t)$ and the assumed measurement uncertainty ε. $d_i(t)$ are the ERT inversion-derived layer resistivities, i = 1, 2, 3 for the three layers and $0 \leq t \leq 30$ days. Φ_{gc} is defined analogous to Φ_{res}, only that $d_i(t)$ are the CO_2 mole fractions, i = 1, 2, for the two observation wells and 11 days $\leq t \leq$ 30 days.

The optimization started using only the ERT-derived electrical resistivities, thus minimizing Φ_{res} only and estimating only the reservoir width. In subsequent steps gas composition data was included and the full objective function Φ was minimized. With this step-wise increase of complexity this study hoped to increase chances of convergence to a stable minimum in the misfit function, honoring both data sets and obtaining accurate parameter estimates.

3.3 ANALYSIS OF TIME-LAPSE ERT DATA

The ERT data was analyzed in a variety of ways in the process of determining the best form to use for the coupled hydrological-geophysical inversion. This section shows different ERT inversion results, including joint inversion with seismic as a structural constraint, inversions for 1-D and 2-D parameter distributions using different regularizations and constraints, and some more recent inversions for 3-D parameter distributions. The results of the ERT time-lapse inversion of Section 3.3.4 are then used in Section 3.4 for coupled hydrological-geophysical inversion.

3.3.1 Mesh Generation and Parameterization

In the following sections (excluding Section 3.3.5) the ERT data is inverted in 3-D using the versatile finite-element inversion program BERT (Günther et al., 2006, www.resisivity.net) with unstructured tetrahedral meshes. These meshes are designed to include arbitrary electrode positions and geometries, such as layer boundaries. Three different meshes were built, all with a domain size of 100 m × 50 m × 100 m and about 30,000 cells. These meshes were refined and extended outwards for the ERT forward calculations.

The first of the three meshes included no internal structure except for the electrode positions. The second mesh included the top and bottom of the reservoir as interfaces, as defined by the self-

potential borehole logs. The third mesh included two additional interfaces within the reservoir based on the porosity borehole logs (Figure 6d), splitting the reservoir into three zones that might have different properties. During the ERT inversion, regularization was applied in the form of spatial smoothing.

3.3.2 Structural Joint ERT and Seismic Inversion (for only two times)

A structural joint inversion of the crosswell seismic and ERT data was performed in early stages of the project (Doetsch et al., 2012a). The structural joint inversion approach was first developed by Gallardo and Meju (2004) and is based on penalizing deviations from zero of the cross-gradient function $\tau = \text{del}(\mathbf{m_1}) \times \text{del}(\mathbf{m_2})$ between models $\mathbf{m_1}$ and $\mathbf{m_2}$. This ensures structural similarity, while not assuming any specific petrophysical relationship between the model parameters. As in the individual time-lapse seismic inversion, this study inverted for changes in seismic velocity. Due to the availability of only one time-lapse seismic data set (pre-injection and post-injection surveys), a single ERT data set was created by averaging 20 days of data after the system reached steady state. The joint inversion results showed a more focused CO_2 plume. As mentioned previously, since the seismic data were only collected before and long after the start of injection, they were ultimately not included in coupled hydrological-geophysical inversions of subsequent sections.

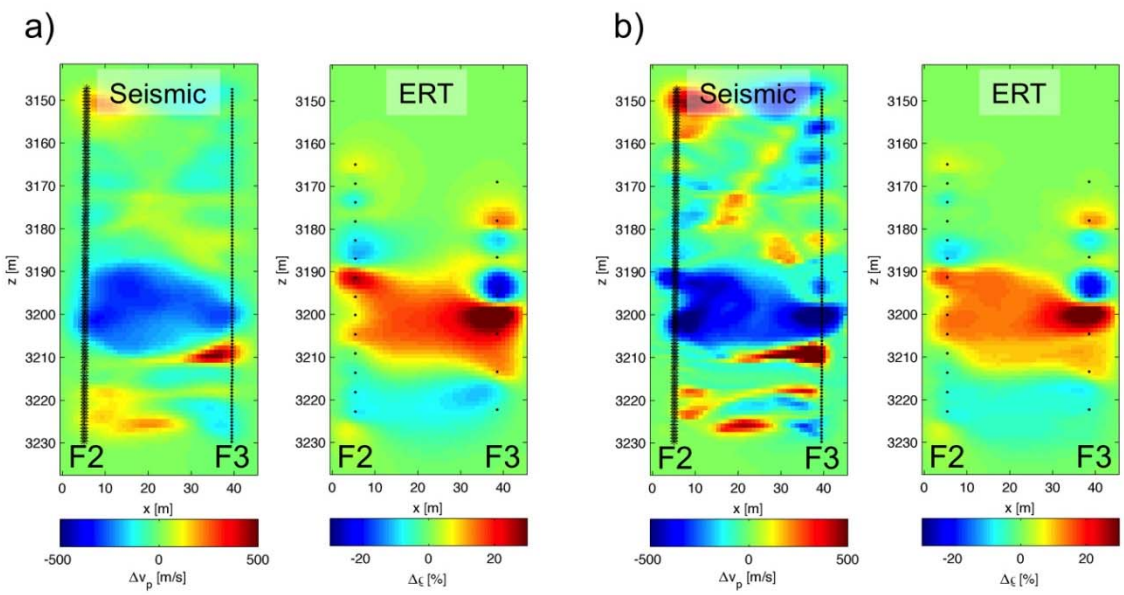

Figure 11: Inversion of seismic and ERT data for changes in seismic velocity and resistivity from baseline to 9 months after the start of CO_2 injection. a) Independent (individual) inversions of each data set. b) Joint inversion of both data sets using cross-gradient structural constraint.

3.3.3 Smooth ERT Inversion for 60 Times

Next the ERT data were inverted using each of the three meshes described in Section 3.3.1. The time-lapse apparent resistivity ratios $\rho_a(t)/\rho_a(0)$ were inverted for 60 two-day periods from 0 to 120 days. The inversion for each time frame started with a homogeneous 1-Ωm model. These models were then updated iteratively until the model explained the data to the assumed error

level or until the data misfit could not be further decreased. The changes in the final models from the 1-Ωm baseline correspond to relative changes in resistivity as a result of CO_2 injection.

A smoothing operator with an anisotropy factor of 0.2 (five times stronger smoothing in horizontal direction) was applied to stabilize the inversion and honor the layered stratigraphy at the site. This regularization was disconnected across the interfaces in Models 2 and 3 to allow independent resistivity variations in the different layers.

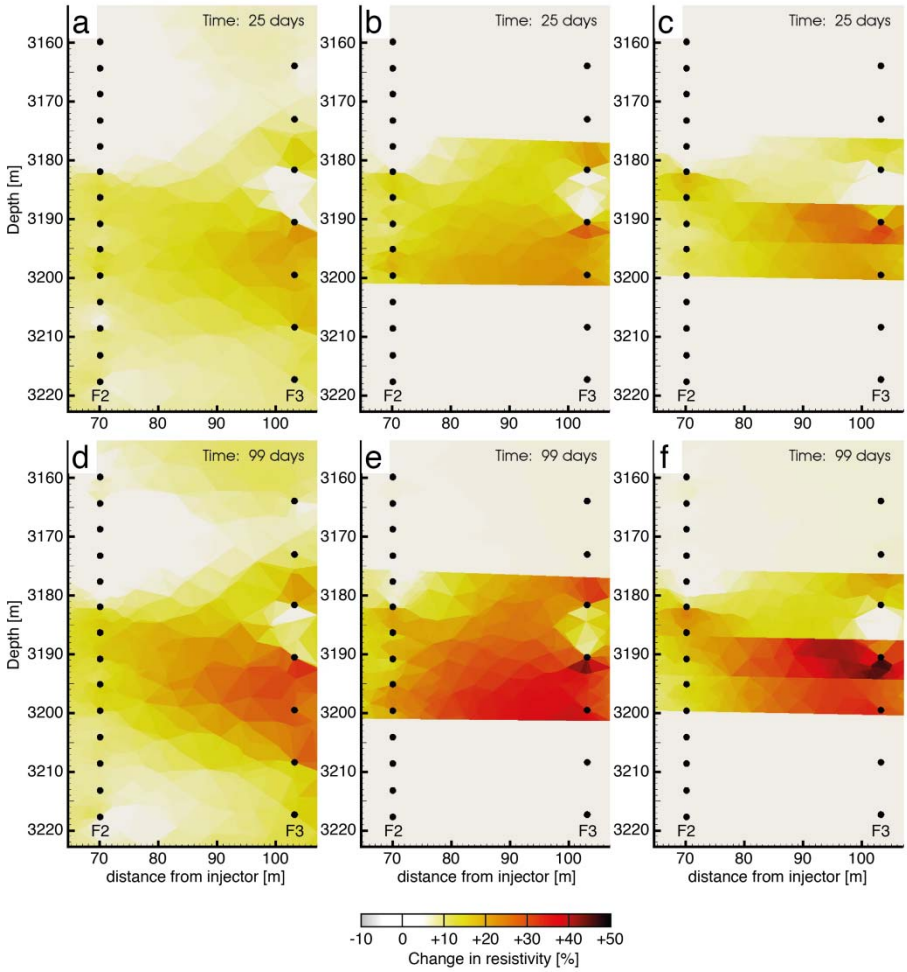

Figure 12: Example time-lapse ERT inversions at 25 days (top) and 99 days (bottom) after the start of CO_2 injection. ERT inversions performed using no spatial constraints are shown for the two respective times (a and d), as are inversions in which the aquifer was decoupled from the overlying and underlying reservoir, with the aquifer assumed to be composed of one layer (b and e) or three layers (c and f). Results are plotted in relative changes to the baseline resistivity distribution. Note that the expected CO_2 flow is from left to right.

Figure 12 shows the inversion results for 25 and 99 days after the beginning of the CO_2 injection. Inversions with all three meshes show the increase of resistivity due to the gas phase occupying the pore space, but there were strong differences in the distribution of resistivity changes. The inversion without any spatial constraints and stationary regularization (Figure 12a and d) does not focus the resistivity changes in the reservoir region, but they were rather smeared over a

larger depth range. This smearing was due to the regularization that prefers smooth models to strongly varying resistivity distributions. This problem was resolved by including the top and bottom of the reservoir in the mesh (Figure 12b and e). The abrupt change across the reservoir boundary was here explicitly allowed and although changes outside the reservoir were allowed in the inversion, they were not reinforced by the data. The three-layer reservoir models (Figure 12c and f) show similar features as the one-layer models, but additionally illustrate larger changes in the lower than in the upper part of the reservoir. As the increase of resistivity was associated with increasing gas saturation, the larger changes in the lower part indicated higher CO_2 and CH_4 accumulation in this region.

While these inversion results illustrate the different changes of resistivity with depth, they appear inadequate to image the horizontal CO_2 propagation in a detailed manner. The CO_2 moves outwards from the injection well F1 at $x = 0$ m and is thus expected to move toward higher x values (from left to right) in Figure 12. Instead, stronger resistivity anomalies were shown close to the observation well F3, and the lateral distribution of the resistivity anomalies did not change much during the experiment. The failure in imaging the lateral movement of the CO_2 and CH_4 was attributed to the limited data quality and the ERT sensitivity distribution for this data set. The ERT sensitivity pattern for crosswell experiments was a complicated function of the relative locations of the involved electrodes, but in general it was high close to the observation wells and low in the center between these wells.

3.3.4 Single-Parameter ERT Inversion for 60 Times

Due to the inability to adequately image the lateral gas movement, it was decided to drastically reduce the number of unknowns in the inversion and invert for a single resistivity value for each of the three reservoir layers for each time step. This approach reduced the number of parameters for each inversion (at each of the 60 time steps) from 30,000 (one resistivity value for each model cell) to four, which included the resistivity outside the reservoir. With only four unknowns, there was no need for regularization during the inversion, because the regularization was implicit in the formulation of the inverse problem.

The same apparent resistivity ratios were inverted as in the smooth inversions, using the three-layer mesh and “single parameter” constraints in the BERT inversion code. At the end of the inversions, the data were fit to the same assumed error level as in the smooth inversions, indicating that this parameterization was a reasonable alternative and that perhaps the data cannot provide higher-resolution information, at least with the assumption of 2-D parameter distributions made for the results in Section 3.3.3.

Figure 13 shows the resulting resistivity time series from the single-parameter inversions for the three layers (solid lines) and compares them with the average resistivities for these layers from the smooth inversion (dashed and dotted lines). All inversion results indicate that the change in resistivity was significantly smaller in the top layer (black) compared to the middle (red) and bottom (blue) layers. The magnitude of the change, however, was underpredicted by almost a factor of two in the unconstrained inversion (dotted lines in Figure 13) for the two lower layers. The constrained smooth inversion that includes the layers (dashed lines) finds slightly larger changes than does the unconstrained inversion. However, changes in resistivity in all smooth inversions were still strongly underpredicted compared to the single parameter inversions. This underprediction of change in resistivity was attributed to the regularization and the limited data quality. The single parameter inversion does not suffer from the regularization problem and thus

gives the best estimate of average change in resistivity for each layer. Therefore, the single parameter inversion results were used as input for the coupled modeling and inversions in Section 3.4.

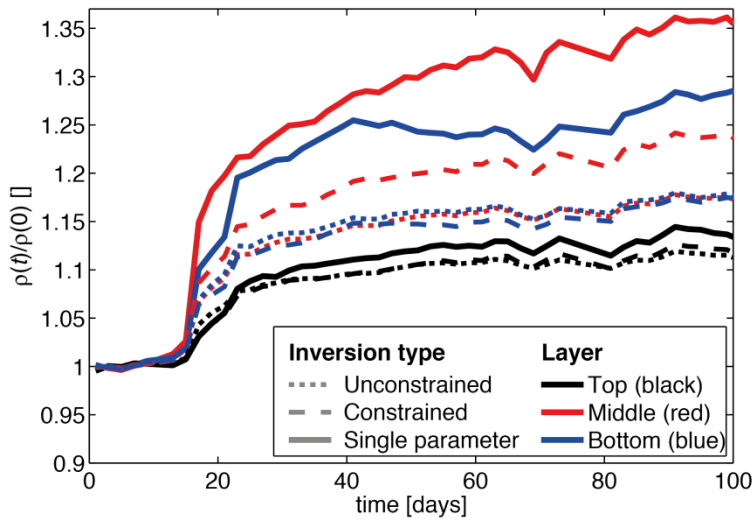

Figure 13: Change in resistivity, normalized by baseline resistivity, inferred from time- lapse ERT inversions. The ERT inversion types are distinguished by line style, colors indicate the different layers. The time series for the unconstrained inversion case was obtained by averaging the estimates in all pixels within the aquifer region at each time (see Figure 12a and d). The constrained inversion case corresponds to the average of the pixels in each of the layers in the three-layer case (see Figure 12c and f). The single parameter inversion used the same mesh as shown in Figure 12c, but only inverted for one parameter for each layer and time-step.

3.3.5 Recent Result: ERT Inversion for 3-D Parameter Distribution using EMGeo

Subsequent to the ERT inversions presented in the previous sections and the coupled hydrological-geophysical inversions of Section 3.4, additional ERT inversions were performed, using EMGeo, in an effort to estimate 3-D distributions and to see if 3-D effects were significant and/or influencing the 2-D interpretations in the previous sections. Figure 14 shows the estimated saturation of CO_2 at a series of times ranging from day 13 to day 103. A slice through the model at y = -3 shows that the center of the plume was not directly in between the observation wells. The isosurface shows interesting variations in 3-D. These results compare favorably with the 2-D results obtained by Carrigan et al. (2013), as shown in Figure 15.

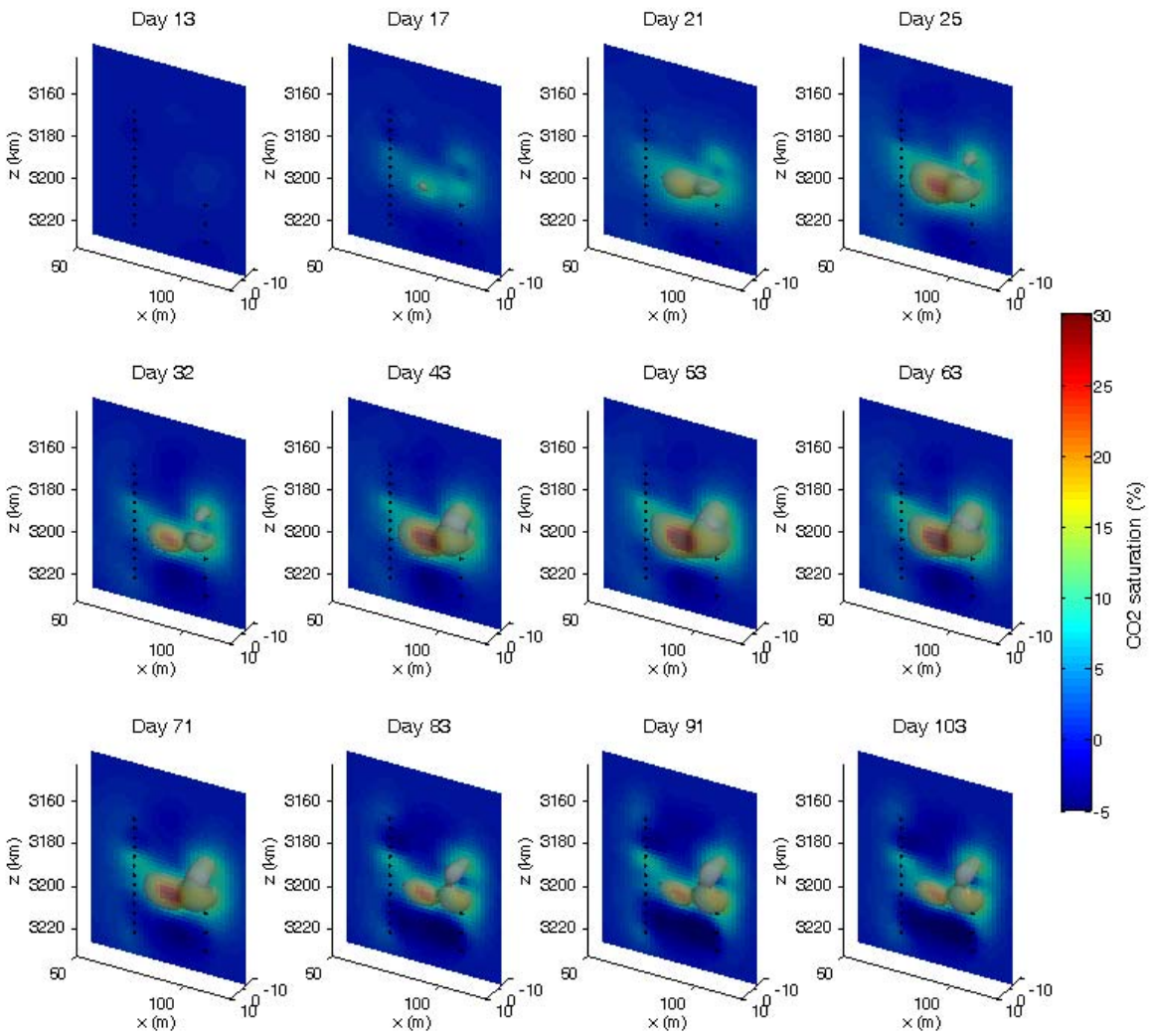

Figure 14: Inversion for 3-D resistivity distribution, converted to CO_2 saturation as function of time.

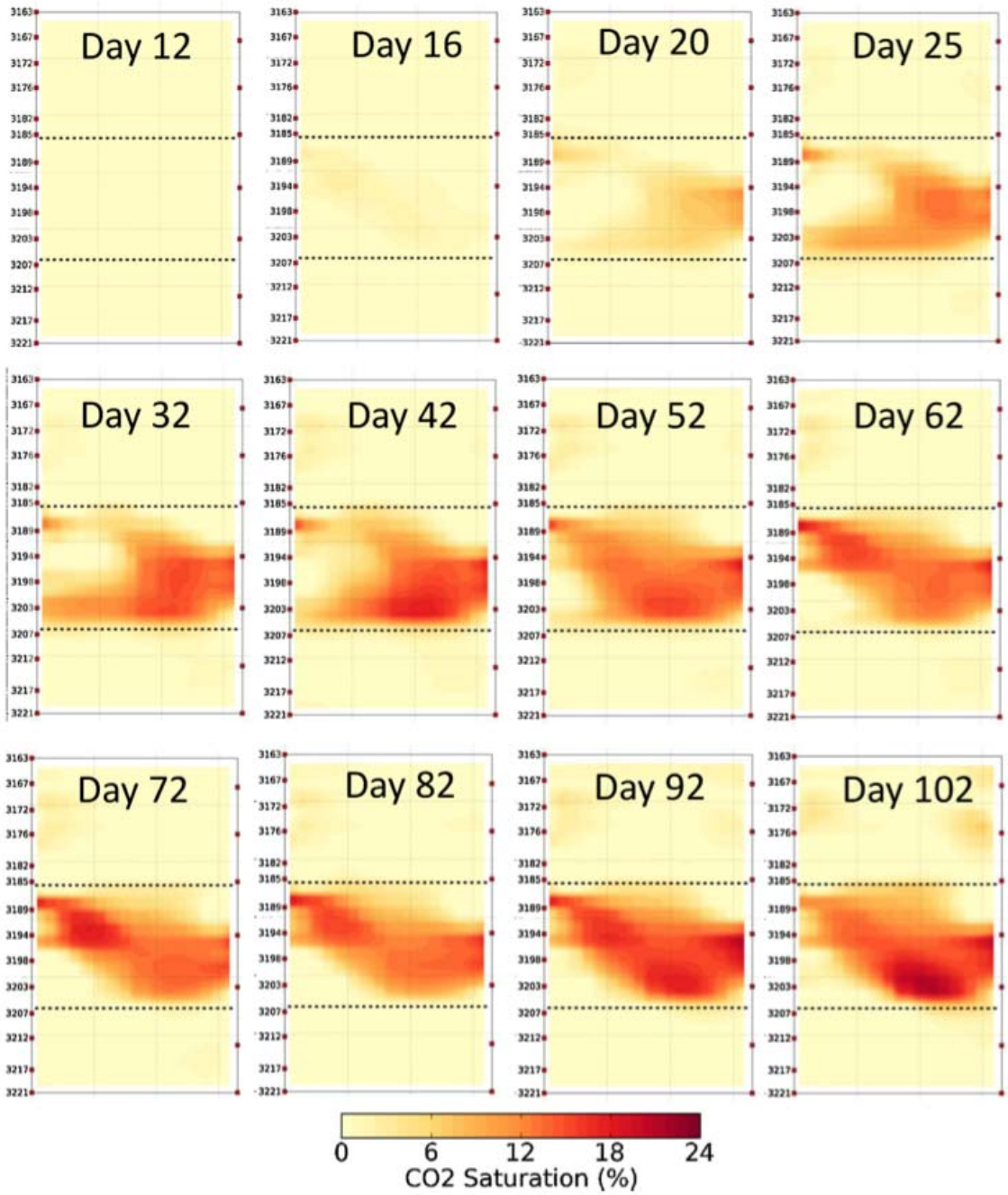

Figure 15: Estimation of CO_2 saturation based on 2-D ERT inversion (Carrigan et al., 2013).

3.4 COUPLED HYDROLOGICAL-GEOPHYSICAL INVERSION RESULTS

The following hydrological modeling used different meshes and geometrical assumptions aimed at identifying the core characteristics of CO_2 migration in the reservoir. This study first considered a radial model, and then used the coupled inversion scheme to optimize the parameters of a model consisting of three 1-D layers and used the inversion results to construct a 3-D model. Sketches of the three meshes are shown in Figure 16. Results from a preliminary inversion using a 3-D model are shown subsequently.

The complex interplay between CO_2 and CH_4 and the two flow paths that were inferred from the gas composition monitoring data (Figure 7) were confirmed by flow and transport simulations. Figure 17 shows CO_2 and CH_4 mole fractions in the gas phase as well as gas saturation for the three layers, as predicted by the inversion model M1 (see Section 3.4.2). The first gas arrival was the CH_4 in the middle layer, followed by the CO_2 in the same layer. The CH_4 in the bottom layer arrives next, reducing the CO_2 mole fraction averaged over the full depth interval of the reservoir. Lastly, the CO_2 in the bottom layer arrived, increasing the depth-averaged CO_2 mole fraction for the remainder of the injection period. The parameter that controls the double arrival of CO_2 in the observation wells was the permeability difference between the middle and the bottom layers. No double arrival can be observed when the permeability was the same, and the time difference between the arrivals increased with increasing permeability difference between the two lower layers.

Figure 17 illustrates that for model M1 (see Section 3.4.2) the gas saturation in the top layer remains very small, so that the contribution from the top layer to the depth-averaged gas composition measured in the boreholes was minor. Note also that the gas saturation stayed relatively low after the arrival of the CH_4 and significantly increased with the arrival of the CO_2.

3.4.1 Simulation with Radial Model

Porosities and layer thicknesses in the initial three-layer radial model (Figure 16a) were based on the porosity log, and permeabilities were based on measurements of sidewall cores in F1 and whole cores in F2. The assigned permeabilities range from k_t = 5 millidarcy (mD) for the top layer to k_m = 249 mD for the middle layer and k_b = 150 mD for the bottom layer (see also Table 1). Figure 18 shows the measured and simulated gas composition and ERT data. The radial model simulation predicted that the gas phase arrives at days 15.3 and 26.8 for F2 and F3, respectively, which was significantly delayed compared to the field data (days 11.0 and 15.0, see also Table 2). Especially the large time difference between the arrivals at F2 and F3 did not agree with the field observations. Increases of model permeability by factors of 10 and 100 shifted the arrival time in F3 by 2–3 days, but could not explain the early arrival in F3 and its short delay compared to F2. The mismatch of the arrivals between field data and simulations was also expressed by high data misfit values that were shown along with the simulation parameters in Table 2.

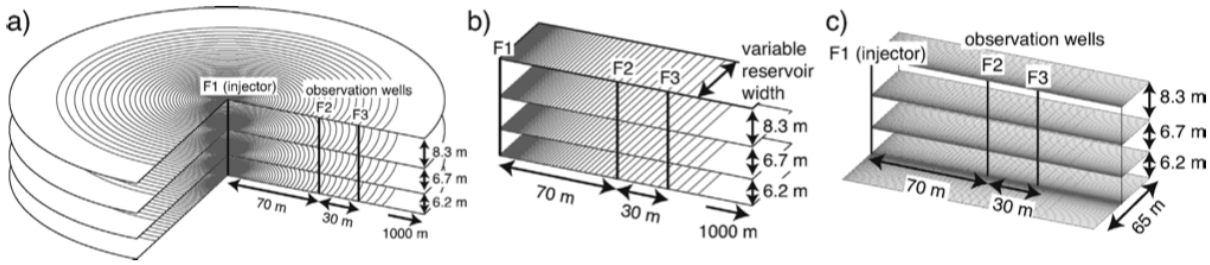

Figure 16: Meshes for the flow and transport modeling in Sections 3.4.1 through 3.4.3. (a) Initial 3-layer radial model, (b) linear model with variable reservoir width, and (c) 3-D model. Model (b) was used in the fully coupled inversion due to its flexibility with variable reservoir width and fast simulation times (1–2 min). The simulation cell size was about a factor of 5 finer than plotted here.

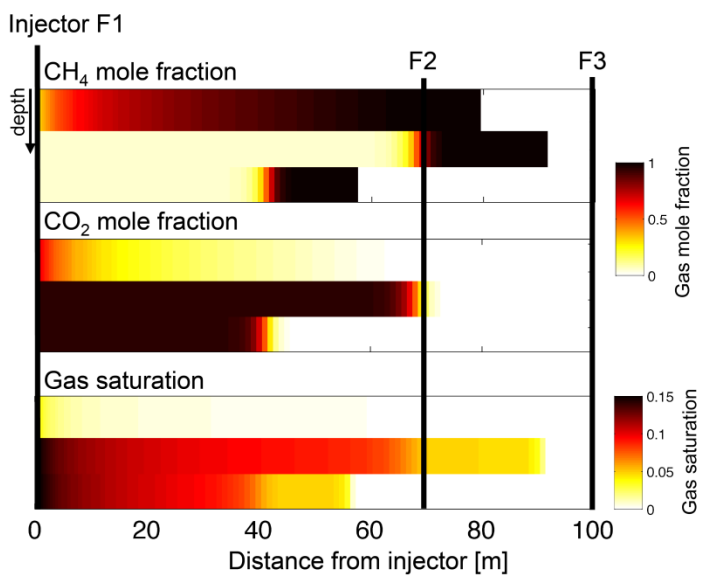

Figure 17: CH_4 and CO_2 gas mole fraction and gas saturation as simulated by model M1 at day 13. Note how the CH_4 arrives first with relatively small gas saturation and that gas saturation increases with the arrival of CO_2. The combination of the two lower layers creates the double arrival of CO_2 and CH_4 that can be observed in the measured (Figure 7) and simulated (Figure 18) data.

Table 1: Parameters and data misfit for the different flow and transport simulations. Model M0 is the starting point of the fully coupled inversion and models M1–M3 are the inversion results. Gray shaded cells mark active parameters and data sets in the different inversions; boldface marks the lowest misfit for each data set. Parameters are given with their estimated uncertainty (standard deviations).

Parameters						Data Misfit		
Models	Width (m)	k_t (mD)	k_m (mD)	k_b (mD)	k_v (mD)	CO_2 rms	Resistivity rms	Total rms
Radial	-	5	249	150	5	11.8	5.0	10.0
M0	200	5	249	150	5	14.7	8.3	12.8
M1	82 ± 4	5	249	150	5	7.7	3.2	6.5
M2	67 ± 3	11 ± 1	97 ± 25	77 ± 29	23 ± 2	9.7	**1.6**	7.9
M3	65 ± 1	5 ± 1	176 ± 8	92 ± 8	11 ± 2	3.3	3.1	3.2
3-D	65	5	176	92	11	**2.4**	4.0	**3.0**

Table 2: Arrival time of the CO_2 gas/supercritical phase at observation wells F2 and F3

Models	CO_2 Arrival Time	
	F2 (days)	F3 (days)
Field	**11.0**	**15.0**
Radial	15.3	26.8
M0	20.2	26.3
M1	12.3	18.5
M2	13.7	20.5
M3	**10.0**	**15.5**
3-D	7.9	12.9

The arrival times measured in the field and the best fit are highlighted in boldface.

The other two parameters with a strong influence on the gas arrival times are porosity and residual liquid saturation. The relative permeability and capillary pressure function used a version of the Brooks–Corey model (Luckner et al., 1989) that was modified to be numerically stable (Finsterle, 1999a). A pore size distribution index of 0.65, a gas entry pressure of 4,000 Pa, and a residual gas saturation of 0.01 was chosen. Tests with different residual liquid saturations S_{lr} showed that only high S_{lr} values were consistent with the ERT-derived resistivities. S_{lr} values lower than 0.5 produced resistivity changes much larger than observed. The best match with the observed change in resistivity was achieved with $S_{lr} = 0.75$. Using this relatively high S_{lr} also helped reduce the arrival time of the gas at the observation wells, which would otherwise be much further from the observed value than described above. In the reservoir, the high S_{lr} could

represent fingering, which is prevalent when a low-viscosity fluid displaces a high-viscosity fluid and which is expected in fluvial deposits with strong local permeability variations.

Changes in porosity also affected the migration velocity of the CO_2, and decreasing porosities reduced the arrival times of the gas phase at the boreholes. For the radial model, reducing the layer porosities to 70% of their initial value improved the predicted breakthrough in F2, but the F3 breakthrough was still delayed by 7 days. While borehole-log derived porosities carry uncertainties, it was determined that they are unlikely to be off by 30%. In the following, especially in the inversions, $S_{lr} = 0.75$ and the borehole-log derived porosities were fixed, while the reservoir permeabilities were varied; ideally, one could invert for all of these parameters simultaneously, but this study found that data coverage and strong parameter correlations did not allow for this.

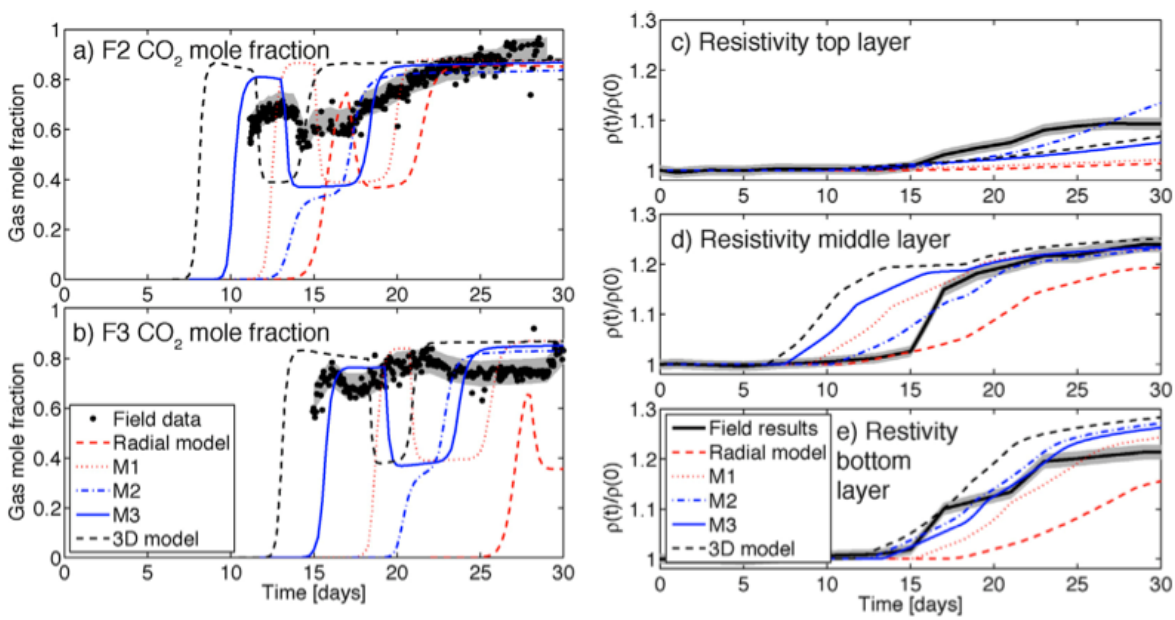

Figure 18: Measured and simulated CO_2 gas mole fraction in (a) F2 and (b) F3, as well as (c–e) inverted and simulated resistivity time series. Note how the match between simulated and measured data (timing and characteristics) is improved through the model development and inversion process. The gray shaded area around the data illustrates the assigned measurement uncertainty (standard deviation).

3.4.2 Inversions with 2-D Models

While parameters in the radial model can be varied so that the arrival at one of the two observation wells can be matched, the time difference between the arrival in F2 and F3 was always overestimated. This is not surprising when looking at the distance-to-arrival-time ratio of 70 m in 11 days and 100 m in 15 days for the respective boreholes, which both correspond to approximately 6.5 m/day. This constant flow velocity indicated a system with 1-D rather than radial characteristics. A three-layer model was created, with each layer consisting of a 1-D model, as shown in Figure 16b. The width of the reservoir, which determines the widths of the three 1-D models, was introduced as an extra parameter that could be varied to fit the data. This reservoir width can be seen as a representative width of the depositional flow channels accessible to CO_2. The run time for the 30-day flow and transport simulation with this model was 1–2

minutes (comparable to the radial model), depending on the parameter set. This short run time enabled detailed parameter testing and inversions.

Reservoir width and permeability were optimized using iTOUGH2 in a step-wise inversion, sequentially adding more data and parameters. The assigned standard deviations were 0.05 for the gas composition data and 0.01 for the ERT-derived resistivities (gray shaded areas in Figure 18). All three inversions (M1–M3) converged in 4–15 iterations. The inversion was started with model M0, using the same permeabilities as in the radial model (see Table 1). In the first inversion, only the reservoir width was optimized against the ERT-derived resistivities, arriving at model M1, with a reservoir width of 82 m. This result was independent of the reservoir width in the starting model, whether it was 20, 100, or 200 m. In the second inversion, M1 was further optimized, by allowing the horizontal permeabilities k_t, k_m, k_b of the three layers and the vertical permeability k_v, controlling flow between the upper two layers, to change. The resulting model M2 fit the ERT-derived resistivities very well (see Figure 18c–e and Table 1), but does not capture the arrival time or double arrival of the CO_2. Including the time-series of CO_2 gas mole fraction at wells F2 and F3 as additional data type in M3 improved the CO_2 data misfit, resulting in both data sets being fit reasonably well. The arrival times of the gas phase in the two observation wells are off by 1 day for F2 and only 0.5 days for F3 (see Table 2). The estimated reservoir width of this final model is 65 m and permeabilities are in the range between 5 mD and 176 mD (Table 1).

3.4.3 Simulation with 3-D Model Parameterized by 2-D Inversion Results

To assess the inversion results, a 3-D model was built on the basis of the parameters estimated in the inversion of the previous section. The model consisted of the same three layers as the other models, but was finely discretized in both horizontal directions (Figure 16c). The 65 m reservoir width was implemented by no-flow boundaries at 32.5 m distance on either side of the injection well. The direction along the borehole line was discretized the same way as the radial and inversion models. The symmetry along the borehole line and perpendicular to it through the injection well was used, so only one quarter of the total domain needed to be simulated. The fine discretization around the injection borehole and the 26,506 model cells increased the simulation run time from 1 to 2 minutes for the radial or inversion models to 20 hours, currently making inversion on a serial computer impractical.

The simulation results for the 3-D model (Figure 18) were similar to the inversion result with the simplified model, but showed one main difference: the arrival time was 2–3 days earlier than in the final inversion result. This delay in the simplified model was attributed to the line-source nature of the injection and the associated smaller pressure increase, which was the driving force for the movement of the CO_2. The 3-D modeling results are 2–3 days off in predicting the gas phase arrival, showing the characteristic double arrival and actually showing the smallest CO_2 gas mole fraction data misfit (Table 1) of all simulations so far.

While the final model reproduced some important features observed in the field data, it was concluded that improvements in the conceptual model, such as introducing spatial permeability heterogeneity within the geological layers, were required to improve results further (see Section 3.3.5).

This 3-D model built on the basis of the inversion results matched the observed data equally well as the inversion result and actually showed the smallest overall data misfit of all simulations

previously considered (Table 1). The low misfit was due to an improved fit of the CO_2 gas mole fraction data (Figure 18a and b), while the ERT data misfit was slightly higher than after the inversion. The effect of a reduced misfit in one data set at the cost of an increased misfit in another data set showed the difficulty of integrating partially inconsistent data. A clear inconsistency between the data sets was the arrival at day 11 of the gas phase in F2 (Figure 18a) and the ERT showing the first increase in resistivity around day 15 (Figure 18c–e).

Evaluation of additional data that was not used in the inversion builds confidence in the validity of this 3-D model: the simulated and observed gas phase arrival times (Table 2) have a mismatch of only 2–3 days for both observation wells. The tracer data measured in the two observation wells and the bottom hole pressure in the injection borehole F1 are shown in Figure 19. The amplitude and peaks of the SF6 tracer were matched reasonably well in both boreholes. The simulated bottom hole pressure (Figure 19b) matched the observations toward the middle of the 30-day period of interest, but was initially too low and too high toward the end. The fact that the pressure data were not included in the inversion is attributed to the higher initial pressure in the observations to a skin effect around the borehole that was confirmed in the field (Hosseini et al., 2013), but not included in this modeling. In addition to the skin effect, the local heterogeneity around F1 was an important factor, as the sidewall cores show much lower permeability than those in F2, which are lower than those in F3.

Performing the coupled inversion using a simplified model with three 1-D layers as opposed to the 3-D model was beneficial due to the decreased simulation run time, which was reduced by a factor of around 600. Recent developments in the parallelization of the TOUGH2 simulator (Zhang et al., 2008) and iTOUGH2 (Finsterle, 1998; Commer et al., 2012) can significantly reduce the simulation and inversion run times, so that inversions with large 3-D models become feasible (see Section 3.3.5).

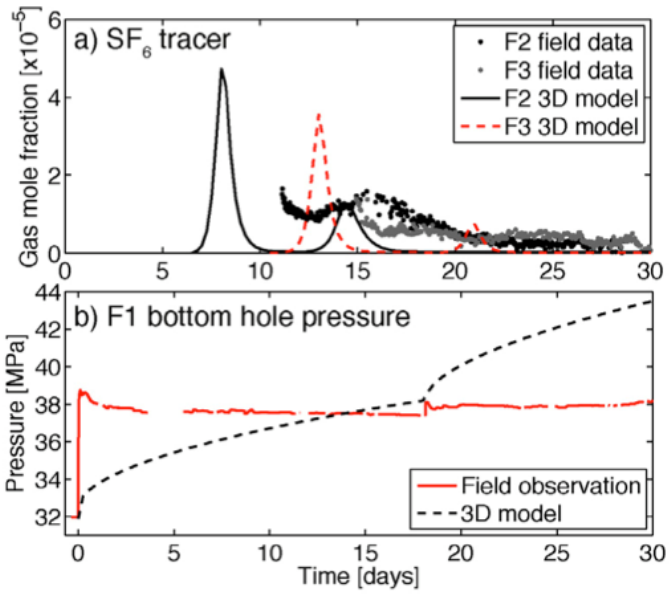

Figure 19: Comparison of additional field data (not used in inversion of this section) and simulation results using the final 3-D model from Section 3.4.2. (a) Gas mole fraction of SF_6 tracer injected at day 3 and (b) bottom hole pressure in the injector F1.

3.4.4 Preliminary Inversion for 3-D Model Parameters

Next, the 3-D model was modified to include a total of 25 unknown parameters, consisting of 22 spatially varying log10 k values in the lower two layers, and three in the upper layer, allowing for heterogeneity in the permeability.

Inversion was accomplished using MPiTOUGH2 (Commer et al., 2013), which enabled parallel inversion runs in which computational improvements to the inversion framework iTOUGH2 were made by replacing the underlying original hydrological simulator TOUGH2 by its parallel counterpart TOUGH2-MP. Allowing for the domain decomposition of a potentially large simulation domain, a new parallel level was added to the concept of distributing multiple forward simulations across parallel processes, thus enabling the efficient exploitation of many-core computing resources. Further, the merge with a parallel geophysical simulator for electrical and electromagnetic data types extended the parameter estimation and error and uncertainty analysis tools of iTOUGH2 to treat a range of hydrogeophysical problems for models that are characterized by high computing demands. These developments were a necessary step to begin addressing the demands resulting from increasing model complexities and a constantly widening range of hydrogeological applications, such as the modeling of CO_2 in the subsurface.

The modified simulation mesh in Figure 20 covers a volume of approximately (x × y × z) 1,051 m × 150 m × 21 m, totaling 36,094 mesh elements and 83,465 connections between them. As before, the system was assumed to be isothermal, and five mass balance equations were solved per mesh element, resulting in a (sparse) matrix system size of 180,470 × 180,470. Element volumes range from 0.05685 to 3,308 m^3, excluding boundary elements. Symmetry considerations allowed for only one quarter of the simulation domain to be modeled and have the purpose of limiting the non-uniqueness problem given by the data sparsity, and to provide a first evaluation whether the introduced lateral heterogeneity improves the data fits of the previous sections. Note that a more realistic 3-D representation of the site is being developed in ongoing efforts.

Numerical time steps varied from an initial size of 0.2 s to 3.4×10^{10} s for the steady-state evaluation until injection begins, and from 1 s to 4×10^4 s for the subsequent transient testing period of 40 days, requiring a total of 525 time steps on average. Figure 21 illustrates the computational requirements for a single forward simulation, where runtimes were evaluated for one to 96 parallel processes. The bulk runtime consisted of the solution of the linear equation systems at each time step, followed by the time for the matrix system's assembly. Each time step further involved updates of the thermophysical properties (indicated by equation-of-state update). All runs used the BiCGSTAB solver of the AZTEC package (see Commer et al., 2013 for details), where the single-threaded run completed after 6.5 hours. For comparison, a simulation was carried out using the original (single-threaded) TOUGH2 direct solver LUBAND (using LU decomposition techniques) (Moridis and Pruess, 1998), which required 55.5 hours on the same compute server. Note that calculations were carried out on a Linux cluster with Intel's Xeons CPU at 2.33 GHz, 12 cores per node, cache size 4,096 KB, Mellanoxs QDR Infiniband network (theoretical limit of 40 GBit/s).

After 24 model updating steps, the Levenberg-Marquardt scheme terminated with the maximum number of 10 trial steps for further misfit reduction. Figure 22 shows the initial model guess (a), final distribution of estimated permeability (b), and estimated parameter sensitivities (c). A comparison between the field data and the data simulated from the inversion result is shown in

Figure 23. The simulated electrical conductivity (EC) (reciprocal of the resistivity) change data (b-d) reproduced the trend of decreasing EC (increasing resistivity) in all layers as the saturation of injected CO_2 increased between the observation wells, though the arrival time of CO_2 is slightly under-predicted in Layer 2. Values of zero before the measured onset were assumed to fill the gap (due to clogging of the U-tube) in the CO_2 mole fraction data. The validity of this assumption was indicated by the match between simulated and measured onset (e, f). The first recorded values of the SF_6 tracer, corresponding to the tail end of the first peak of the tracer arrival, were also reproduced by the inversion (g, h). However, it was found that the overall inversion progress benefits from strongly down-weighting the SF_6 tracer data, to a degree that their influence on the inversion is negligible. This indicates that this model parameterization may still be inadequate to explain the complicated arrival history of all data sets simultaneously.

The total fitting error is reduced by 80% (with respect to the starting model's data fit). Table 3 summarizes the starting (Iteration 0) and final (Iteration 24) errors for each of the 7 individual data sets, their average data standard deviations (in % of the data amplitudes), and their number of data points. While the largest error reduction was attributed to the CO_2 mole fraction data, most of the complexity of the peaks that follow the first arrival was not well reproduced, also indicating the need for further refinement of the inversion. This was likely to also further improve the EC change data fits. Ongoing research aspects include improved parameterization of the model, analysis of the sensitivity of the results to the initial guesses, and construction of a fully-3-D numerical grid for the forward simulations.

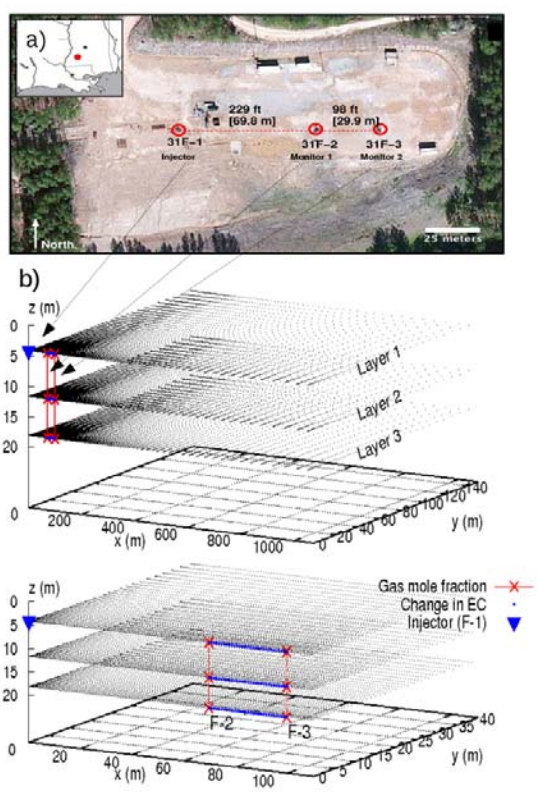

Figure 20: Field site (top) and corresponding numerical grid used in Section 3.4.4 shown in its entirety (middle) and zoomed in around the wells (bottom).

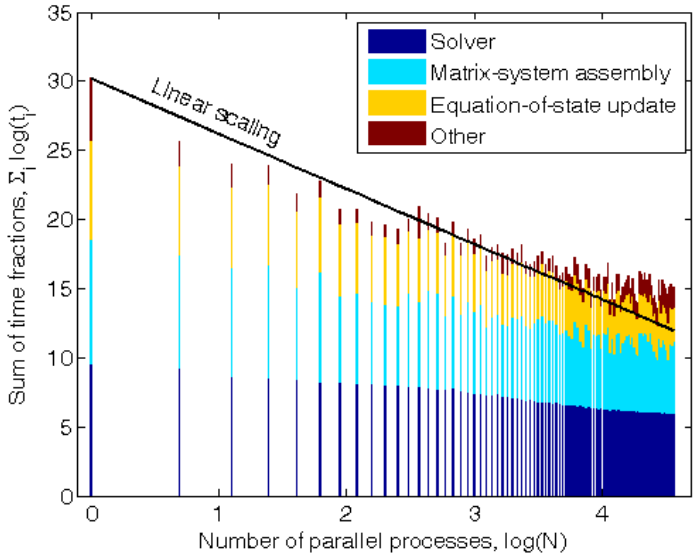

Figure 21: Computing times versus resources for a single forward simulation of the Cranfield 3-D model, using from 1 to 96 parallel processes (see Commer et al., 2013).

Table 3: Data fitting errors calculated from the starting model (Iteration 0) and final model (Iteration 24) for each of the 7 individual data sets (see Commer et al., 2013)

Data set	ε (Iteration 0)	ε (Iteration 24)	Average standard deviation (%)	Number of data points
Layer 1, change in EC	5.65	1.63	1.05	19
Layer 2, change in EC	7.51	10.57	1.15	19
Layer 3, change in EC	4.05	2.54	1.12	19
Well F-2, CO_2	8.40	2.67	5.75	44
Well F-3, CO_2	54.67	2.02	5.66	40
Well F-2, SF_6 tracer	1.78	2.26	96.73	42
Well F-3, SF_6 tracer	0.63	0.62	126.73	36

Note: The average data standard deviations (calculated as a percentage of the data amplitudes) in column 3 highlight the relative weight on the inversion process that is attributed to each data set.

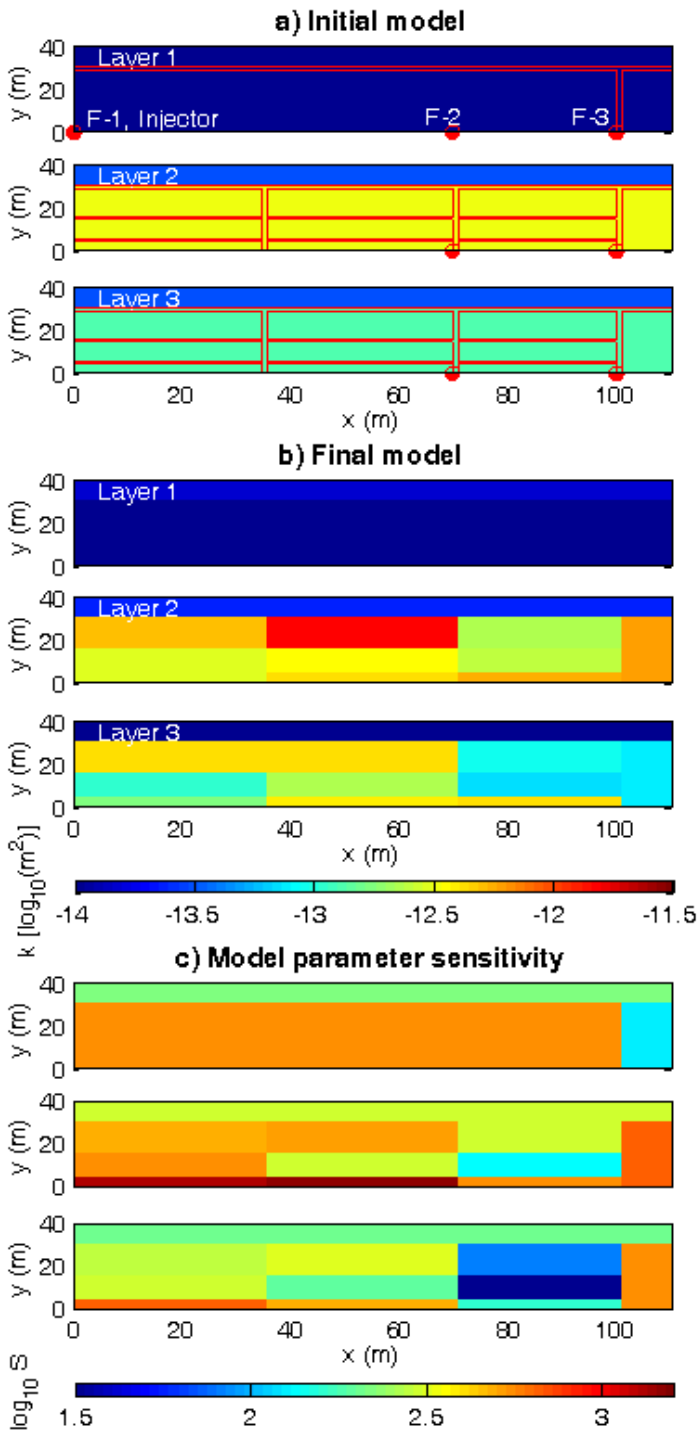

Figure 22: (a) Starting model guess, (b) final inversion result, and (c) estimated dimensionless parameter sensitivities of the 3-D inversion result of Section 3.4.4. The lateral model parameterization of each layer is outlined in (a). Altogether 25 horizontal permeability parameters are distributed over all three layers. Note the spatially truncated representation in order to focus on the fine parameterization of the region around the wells. See Commer et al. (2013) for details on calculation of the parameter sensitivities.

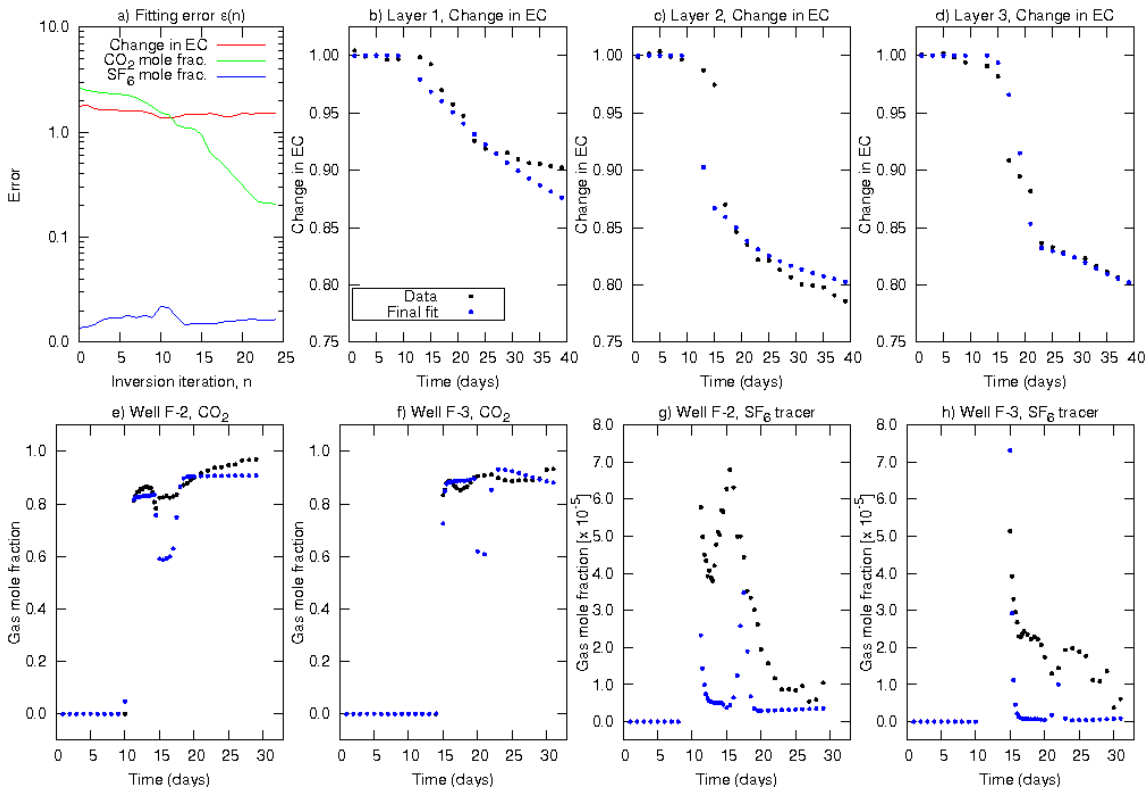

Figure 23: Data fits calculated from the preliminary 3-D inversion result of Section 3.4.4. (a) The total error contributions calculated for each inversion iteration n, for the three different data types (change in EC, CO_2 gas mole fraction, and SF_6 tracer gas mole fraction). Observations and final data fits calculated from the model of inversion iteration are shown for the individual data sets: (b-d) EC change data, (e,f) CO_2 gas mole fractions, and (g,h) SF_6 tracer gas mole fractions.

3.5 DISCUSSION

The results of the ERT inversion (Section 3.3) show both the high potential and the limitations of electrical resistance monitoring of CO_2 in deep reservoirs. The main advantage is clearly the sensitivity to changes in gas saturation at the inter-borehole scale that are otherwise very difficult to monitor. The challenges in the specific case of the Cranfield field experiment relate to the complex and involved field effort and the comparably poor data quality. Both factors are due to the harsh conditions existing at the site and complicated deployments at depths greater than 3,000 m. The ability to image the front of the gas phase moving between the two boreholes would have helped the characterization of the reservoir immensely, but was unfortunately not possible in this specific case due to the poor signal to noise ratio and available electrode geometry. Future experiments in shallower environments with improved signal to noise ratio will have a good chance of success in this respect, building on the experimental experience gained here.

The constrained inversions (Figure 12) showed how important structural information can be for a meaningful inversion of ERT data. Moreover, the single parameter inversion (Figure 13) demonstrated a way to retrieve dependable time series of the average change in resistivity for the

three reservoir layers–despite limitations in data quality. The time-lapse formulation of the ERT inversion and the petrophysical relationship also minimized uncertainties in the estimation of gas saturation change. Only Archie's saturation exponent *n* in Equation 2 needs to be assumed or inverted.

The model development process showed that a radial model was not adequate for simulating the Cranfield reservoir and reproducing the ERT and gas composition data. The main difference between the radial model and the inversion model, which consisted of three layers of 1-D models, was the limited reservoir width; using the latter model for inversion was inspired by the fact that the same phase-front velocity between the injection well and the two observation wells were observed, which indicated a linear rather than a radial flow field. In the reservoir formation (the Tuscaloosa D/E sands), this limited reservoir width probably represents braided flow channels with interbedded low permeability zones. The relative timing of the gas phase arrival in the two observation wells was reproduced much better by the limited-width model, indicating that the general flow behavior was captured. Another explanation for the early arrival in F3 could be a fast flow path that was accessed by F3 and not by (i.e., bypasses) F2. However, this hypothesis cannot be tested with the available data.

The coupled inversion of ERT-derived resistivities and gas composition data showed that the available data could be reasonably matched by optimizing reservoir width and permeabilities. Including ERT data reduced the non-uniqueness of the inverse problem and helped avoid local minima in the objective function. The gas composition data added additional information about the detailed arrivals at the wells. Results of inversions with the gas composition data alone were strongly dependent on the permeability starting values and did not give reliable results. The step-wise inversion, where more data and parameters were sequentially added, was important to ensure convergence to the global minimum. The layer permeabilities were chosen as the main inversion parameters, knowing that changes in porosity or residual liquid saturation S_{lr} also strongly influence the flow velocities. The porosities in these models are derived from borehole logs and the residual liquid saturation $S_{lr} = 0.75$ was constrained by the amplitude of the change in resistivity. However, the uncertainty of the S_{lr} value was significant and the borehole porosity logs could also be off by a few percent. The permeabilities of 176 mD and 92 mD in the lower two layers of the final inversion result agree with core permeability estimates from F2 (most between 10 mD and 100 mD, with a mean of 31 mD; Lu et al., 2013) and F3 (most between 1 mD and 1,000 mD, with a mean of 148 mD; Lu et al., 2013) and 400 mD derived from a hydraulic well-test between F1 and F2 (Hosseini et al., 2013).

The 3-D model built on the basis of the inversion results matched the observed data well (Section 3.4.3), and the misfit was reduced even further when allowing for 3-D heterogeneity (Section 3.4.4). Ongoing efforts include coupled hydrological-geophysical inversion with direct resistivity data, rather than the reduced form as was considered in this study.

3.6 CONCLUSIONS

This study investigated how electrical resistance monitoring data could be used for constraining models for simulation of the flow and transport of CO_2 at the SECARB pilot site in Cranfield, Mississippi. The coupled modeling and inversion scheme of iTOUGH2 was used, where simulation results were directly compared to available geophysical and hydrological data. In this example, the ERT monitoring data was first inverted for changes of subsurface resistivity. The increasing resistivity was imaged due to the arriving gas phase CO_2 and found that these

inversions were strongly improved by including structural information, e.g., from borehole log data. Due to data quality limitations, the fine-scale CO_2 movement through the reservoir could not be imaged, but time series of average resistivity in the three reservoir layers showed a clear and consistent increase in resistivity due to the increase in gas saturation.

Simulations were tested in the hydrological model development by comparing predicted and measured (inverted) resistivities in three reservoir layers and gas composition data from two observation wells, which determined the following:

1. The reservoir could not be properly described with a radial model; flow characteristics (e.g., arrival times versus distance) indicated linear flow. Linear flow was implemented by limiting the reservoir width. This effective reservoir width (with best estimate of 65 m) represents the flow channels in the fluvial deposits. Out-of-plane preferential flow paths could give a similar response, this hypothesis could not be satisfactorily assessed with the available 2-D data.
2. ERT and gas composition data could be used to invert for the layer permeabilities and reservoir width of a simplified model
3. ERT data was crucial in the inversion due to the large measurement footprint and direct link to gas saturation. Inversions of gas composition data alone did not give reliable results.
4. A 3-D model built on the basis of the inversion result provided some confirmation of the parameter estimates since the ERT, CO_2 gas mole fraction and tracer data were fit reasonably well. A subsequent coupled 3-D inversion allowed for 3-D heterogeneity and an improved data fit.
5. These findings showed the potential benefit from monitoring CO_2 migration with ERT data, as well as potential limitations due to poor data quality and structural resolution
6. Fully coupled inversion of time-lapse ERT data with the directly measured resistance values rather than the reduced form or ERT data for detailed 3-D distributions of permeability will be an important extension of this work

This page intentionally left blank.

4. REFERENCES

Ajo-Franklin, J. B.; Peterson, J.; Doetsch, J.; Daley, T. M. High-resolution characterization of a CO_2 plume using crosswell seismic tomography: Cranfield, MS. *Int. J. Greenh. Gas Control* **2013,** *18*, 497–509. http://dx.doi.org/10.1016/j.ijggc.2012.12.018

al Hagrey, S. A. 2-D optimized electrode arrays for borehole resistivity tomography and CO_2 sequestration modelling. *Pure Appl. Geophys.* **2012,** *169*, 1283–1292.

Archie, G. E. The electrical resistivity log as an aid in determining some reservoir characteristics. *Trans. Am. Inst. Min., Metall. Pet. Eng.* **1942,** *146*, 54–62.

Benson, S. M.; Cook, P. J.; et al. Underground geological storage of carbon dioxide. In *Intergovernmental Panel on Climate Change Special Report on Carbon Dioxide Capture and Storage*; Metz, B., Davidson, O., Coninck, H. D., Loos, M., Meyer, L., Eds.; Cambridge University Press: New York, 2005.

Bergmann, P.; Schmidt-Hattenberger, C.; Kiessling, D.; Rücker, C.; Labitzke, T.; Henninges, J.; Baumann, G.; Schütt, H. Surface-downhole electrical resistivity tomography applied to monitoring of CO_2 storage at Ketzin, Germany. *Geophysics* **2012,** *77*, B253–B267.

Butsch, R.; Brown, A. L.; Bryans, B.; Kolb, C. The value of integration – lessons learned through comparing and contrasting monitoring technologies deployed at Cranfield. *Int. J. Greenh. Gas Control* **2013,** 18, 409–420. http://dx.doi.org/10.1016/j.ijggc.2013.06.010

Carrigan, C. R.; Ramirez, A. L.; Newmark, L.; Aines, R.; Friedmann, S. J. Application of ERT for tracking CO_2 plume growth and movement at the SECARB Cranfield site. In *8th Annual Conference on Carbon Capture & Sequestration*, Pittsburgh, PA; Lawrence Livermore National Laboratory Report LLNL-CONF- 412618; 2009.

Carrigan, C. R.; Yang, X.; LaBrecque, D. J.; Larsen, D.; Freeman, D.; Ramirez, A. L.; Daily, W.; Aines, R.; Newmark, R.; Friedmann, J.; Hovorka, S. Electrical resistance tomographic monitoring of CO_2 movement in deep geologic reservoirs. *Int. J. Greenh. Gas Control* **2013,** *18*, 401–408. http://dx.doi.org/10.1016/j.ijggc.2013.04.016

Christensen, N. B.; Sherlock, D.; Dodds, K. Monitoring CO_2 injection with crosshole electrical resistivity tomography. *Explor. Geophys.* **2006,** *37*, 44–49.

Commer, M.; Kowalsky, M. B.; Finsterle, S.; Newman, G. A. Advances in hydrogeophysical joint inversion. In *TOUGH Symposium, Lawrence Berkeley National Laboratory*, Berkeley, CA, 2012.

Commer, M.; Kowalsky, M. B.; Doetsch, J.; Newman, G.; Finsterle, S. MPiTOUGH2: A parallel parameter estimation framework for hydrological and hydrogeophysical applications. *Comput. Geosci.* **2013**. http://dx.doi.org/10.1016/j.cageo.2013.06.011

Commer, M.; Newman, G. A.; Williams, K. H.; Hubbard, S. S. Three-dimensional induced polarization data inversion for complex resistivity. *Geophysics* **2011,** *76*, F157–171.

Coscia, I.; Linde, N.; Greenhalgh, S.; Vogt, T.; Green, A. Estimating traveltimes and groundwater flow patterns using 3-D time-lapse crosshole ERT imaging of electrical resistivity fluctuations induced by infiltrating river water. *Geophysics* **2012,** *77*, E239–E250.

Dafflon, B.; Wu, Y.; Hubbard, S. S.; Birkholzer, J. T.; Daley, T. M.; Pugh, J. D.; Peterson, J. E.; Trautz, R. C. Monitoring CO_2 intrusion and associated geochemical transformations in a shallow groundwater system using complex electrical methods. *Environ. Sci. Technol.* **2013,** *47*, 314–321.

Daily, W.; Owen, E. Cross-borehole resistivity tomography. *Geophysics* **1991,** *56*, 1228–1235.

Daily, W.; Ramirez, A. Electrical-resistance tomography during in-situ trichloroethylene remediation at the savanna river site. *Pure Appl. Geophys.* **1995,** *33*, 239–249.

Daley, T. M.; Ajo-Franklin, J. B.; Doughty, C. Constraining the reservoir model of an injected CO_2 plume with crosswell CASSM at the Frio-II brine pilot. *Int. J. Greenh. Gas Control* **2011,** *5*, 1022–1030.

Daley, T. M.; Myer, L. R.; Peterson, J. E.; Majer, E. L.; Hoversten, G. M. Time-lapse crosswell seismic and VSP monitoring of injected CO_2 in a brine aquifer. *Environ. Geol.* **2008,** *54*, 1657–1665.

Daley, T. M.; Solbau, R. D.; Ajo-Franklin, J. B.; Benson, S. M. Continuous active-source seismic monitoring of CO_2 injection in a brine aquifer. *Geophysics* **2007,** *72*, A57–A61.

Doherty, J., PEST: Model-Independent Parameter Estimation, *Watermark Numerical Computing*, Brisbane, Australia, 2008.

Doetsch, J.; Kowalsky, M. B.; Doughty, C.; Finsterle, S.; Ajo-Franklin, J. B.; Yang, X.; Carrigan, C. R.; Daley, T. M. Towards fully coupled hydrogeophysical inversion of CO_2 migration data in a deep saline aquifer, SEG-AGU 2012 Hydrogeophysics Workshop, Boise, ID, July 8–11, 2012a.

Doetsch, J.; Kowalsky, M. B.; Doughty, C.; Finsterle, S.; Ajo-Franklin, J. B.; Carrigan, C. R.; Yang, X.; Hovorka, S. D.; Daley, T. M. Constraining CO_2 simulations by coupled modeling and inversion of electrical resistance and gas composition data. *Int. J. Greenh. Gas Control* **2013,** *18*, 510–522. http://dx.doi.org/10.1016/j.ijggc.2013.04.011

Doetsch, J.; Kowalsky, M. B.; Doughty, C.; Finsterle, S.; Ajo-Franklin, J. B.; Yang, X.; Carrigan, C. R.; Daily, T. M. Structural and fully coupled joint inversion for CO_2 migration monitoring. 2012 Fall Meeting, AGU, San Francisco, CA, Dec 3–7, 2012b.

Doetsch, J.; Kowalsky, M. B.; Finsterle, S.; Doughty, C.; Ajo-Franklin, J. B.; Daley, T. M. Geophysical data improve stability and convergence of hydrological property estimation: A synthetic CO_2 injection study. Proc. TOUGH Symp. 2012, Sept 17–19, Berkeley, CA, 2012c.

Doetsch, J.; Linde, N.; Binley, A. Structural joint inversion of time-lapse cross-hole ERT and GPR travel time data. *Geophys. Res. Lett.* **2010,** *37*, L24404.

Doetsch, J.; Linde, N.; Pessognelli, M.; Green, A. G.; Günther, T. Constraining 3-D electrical resistance tomography with GPR reflection data for improved aquifer characterization. *J. of Applied Geophysics* **2012,** *78*, 68–76.

Doughty, C.; Freifeld, B. M. Modeling CO_2 injection at Cranfield, Mississippi: Investigation of methane and temperature effects. *Greenh. Gas Sci. Technol.* **2013,** *3*, 475–490. doi:10.1002/ghg.1363

Ellis, R. G.; Oldenburg, D. W. Applied geophysical inversion. *Geophys. J. Int.* **1994,** *116*, 5–11.

Finsterle, S. *Parallelization of iTOUGH2 Using PVM*; Report LBNL-42261; Lawrence Berkeley National Laboratory, Berkeley, CA, 1998.

Finsterle, S. *iTOUGH2 Command Reference*; Report LBNL-40041; Lawrence Berkeley National Laboratory, Berkeley, CA, 1999a.

Finsterle, S. *iTOUGH2 User's Guide*; Report LBNL-40040; Lawrence Berkeley National Laboratory, Berkeley, CA, 1999b.

Finsterle, S. Multiphase inverse modeling: Review and iTOUGH2 applications. *Vadose Zone J.* **2004,** *3*, 747–762.

Finsterle, S. *iTOUGH2 Universal Optimization Using the PEST Protocol*; Report LBNL-3698E; Lawrence Berkeley National Laboratory, Berkeley, CA, 2010.

Finsterle, S.; Kowalsky, M. B. Joint hydrological–geophysical inversion for soil structure identification. *Vadose Zone J.* **2008,** *7*, 287.

Finsterle, S.; Sonnenthal, E. L.; Spycher, N. Advances in subsurface modeling using the TOUGH suite of simulators. *Comput. Geosci.* **2013**. http://dx.doi.org/10.1016/j.cageo.2013.06.009

Finsterle, S.; Zhang, Y. Solving iTOUGH2 simulation and optimization problems using the PEST protocol. *Environ. Modelling & Software* **2011,** *26*, 959–968.

Freifeld, B. M.; Trautz, R. C.; Kharaka, Y. K.; Phelps, T. J.; Myer, L. R.; Hovorka, S. D.; Collins, D. J. The U-tube: a novel system for acquiring borehole fluid samples from a deep geologic CO_2 sequestration experiment. *J. Geophys. Res.* **2005,** *110*, B10203.

Gallardo, L.A.; Meju, M. A. Joint two-dimensional dc resistivity and seismic traveltime inversion with cross-gradients constraints. *J. Geophys. Res.* **2004,** *109*, B03311. doi:10.1029/2003JB002716.

Giese, R.; Henninges, J.; Lüth, S.; Morozova, D.; Schmidt-Hattenberger, C.; Würdemann, H.; Zimmer, M.; Cosma, C.; Juhlin, C. Monitoring at the CO_2 SINK site: a concept integrating geophysics, geochemistry and microbiology. *Energy Procedia* **2009,** *1*, 2251–2259.

Günther, T. *Inversion methods and resolution analysis for the 2-D/3-D reconstruction of resistivity structures from DC measurements*. TU Bergakademie Freiberg, 2004. http://webdoc.sub.gwdg.de/ebook/ serien/aa/Freiberger Diss Online/259.pdf

Günther, T.; Rücker, C.; Spitzer, K. Three-dimensional modelling and inversion of dc resistivity data incorporating topography – II. Inversion. *Geophys. J. Int.* **2006,** *166*, 506–517.

Hinnell, A. C.; Ferré, T. P. A.; Vrugt, J. A.; Huisman, J. A.; Moysey, S.; Rings, J.; Kowalsky, M.B. Improved extraction of hydrologic information from geophysical data through coupled hydrogeophysical inversion. *Water Resour. Res.* **2010,** *46*, W00D40.

Hovorka, S. D.; Benson, S. M.; Doughty, C.; Freifeld, B. M.; Sakurai, S.; Daley, T. M.; Kharaka, Y..; Holtz, M. H.; Trautz, R. C.; Nance, H. S.; Myer, L. R.; Knauss, K. G. Measuring permanence of CO_2 storage in saline formations: the Frio experiment. *Environ. Geosci.* **2006,** *13*, 105–121.

Hovorka, S. D.; Meckel, T. A.; Trevino, R. H.; Lu, J.; Nicot, J.-P.; Choi, J.-W.; Freeman, D.; Cook, P.; Daley, T. M.; Ajo-Franklin, J. B.; Freifeld, B. M.; Doughty, C.; Carrigan, C. R.; Brecque, D. L.; Kharaka, Y. K.; Thordsen, J. J.; Phelps, T. J.; Yang, C.; Romanak, K. D.; Zhang, T.; Holt, R. M.; Lindler, J. S.; Butsch, R. J. Monitoring a large volume CO_2 injection: year two results from SECARB project at Denbury's Cranfield, Mississippi, USA. *Energy Procedia* **2011,** *4*, 3478–3485.

Hosseini, S. A.; Lashgari, H.; Choi, J. W.; Nicot, J.-P.; Lu, J.; Hovorka, S. D. Static and dynamic reservoir modeling for geological CO_2 sequestration at Cranfield, Mississippi, U.S.A. *Int. J. Greenh. Gas Control* **2013,** *18*, 449–462. http://dx.doi.org/10.1016/j.ijggc.2012.11.009

Huisman, J. A.; Rings, J.; Vrugt, J. A.; Sorg, J.; Vereecken, H. Hydraulic properties of a model dike from coupled Bayesian and multi-criteria hydrogeophysical inversion. *J. Hydrol.* **2010**, *380*, 62–73.

Karypsis, G.; Kumar, V. METIS. *A software package for partitioning unstructured graphs, partitioning meshes, and computing fill-reducing orderings of sparse matrices, V4.0*; Technical Report, Department of Computer Science, University of Minnesota, 1998.

Kowalsky, M. B.; Birkholzer, J.; Peterson, J.; Finsterle, S.; Mukhopadhyay, S.; Tsang, Y. Sensitivity analysis for joint inversion of GPR and thermal-hydrological data from a large-scale underground heater test, *Nucl. Technol.*, **2008,** *164*, 196–206.

Kowalsky, M. B.; Commer, M.; Ajo Franklin, J. B.; Doughty, C.; Daley, T. M.; Finsterle, S. *Feasibility of coupled hydrogeophysical inversion for characterization and monitoring of subsurface CO_2 injection*, 2011 Fall Meeting, AGU, San Francisco, CA, Dec 5–9, 2011a; Abstract H42F-02.

Kowalsky, M. B.; Finsterle, S.; Peterson, J.; Hubbard, S.; Rubin, Y.; Majer, E.; Ward, A.; Gee, G. Estimation of field-scale soil hydraulic and dielectric parameters through joint inversion of GPR and hydrological data. *Water Resour. Res.* **2005,** *41*, W11425.

Kowalsky, M. B.; Finsterle, S.; Rubin, Y. Estimating flow parameter distributions using ground-penetrating radar and hydrological measurements during transient flow in the vadose zone, *Adv. Water Resour.* **2004,** *27*, 583–599.

Kowalsky, M. B.; Gasperikova, E.; Finsterle, S.; Watson, D.; Baker, G.; Hubbard, S. S. Coupled modeling of hydrogeochemical and electrical resistivity data for exploring the impact of recharge on subsurface contamination. *Water Resour. Res.* **2011b,** *47*, W02509.

Kowalsky, M. B.; Nakagawa, S.; Moridis, G. J. Feasibility of monitoring gas hydrate production with time-lapse vertical seismic profiling, *SPE J.* **2010,** *15*, 634-645. SPE-132508-PA. doi: 10.2118/132508-PA.

Landrot, G.; Ajo-Franklin, J. B.; Yang, L.; Cabrini, S.; Steefel, C. I. Measurement of accessible reactive surface area in a sandstone, with application to CO_2 mineralization. *Chem. Geol.* **2012,** *318–319*, 113–125.

Levenberg, K. A method for the solution of certain nonlinear problems in least squares. *The Quarterly of Applied Mathematics* **1944,** *2*, 164–168.

Lu, J.; Cook, P. J.; Hosseini, S. A.; Yang, C.; Romanak, K. D.; Zhang, T.; Freifeld, B. M.; Smyth, R.C.; Zeng, H.; Hovorka, S. D. Complex fluid flow revealed by monitoring CO_2 injection in a fluvial formation. *J. Geophys. Res.* **2012a,** *117*, B03208.

Lu, J.; Kharaka, Y. K.; Thordsen, J.J.; Horita, J.; Karamalidis, A.; Griffith, C.; Hakala, J.A.; Ambats, G.; Cole, D.R.; Phelps, T. J.; Manning, M. A.; Cook, P. J.; Hovorka, S.D. CO_2–rock–brine interactions in Lower Tuscaloosa Formation at Cranfield CO_2 sequestration site, Mississippi, U.S.A. *Chem. Geol.* **2012b,** *291*, 269–277.

Lu, J.; Kordi, M.; Hovorka, S. D.; Meckel, T. A.; Christopher, C. A. Reservoir characterization and complications for trapping mechanisms at Cranfield CO_2 injection site. *Int. J. Greenh. Gas Control* **2013,** *18*, 361–374. http://dx.doi.org/10.1016/j.ijggc.2012.10.007

Luckner, L.; Van Genuchten, M. T.; Nielsen, D. R. A consistent set of parametric models for the two-phase flow of immiscible fluids in the subsurface. *Water Resources Research* **1989,** *25*, 2187–2193.

Marquardt, D. W. An algorithm for least squares estimation of nonlinear parameters. *SIAM Journal of Applied Mathematics* **1963,** *11*, 431–441.

Moridis, G.; Pruess, K. T2SOLV: An enhanced package of solvers for the TOUGH2 family of reservoir simulation codes. *Geothermics* **1998,** *27*, 415-444.

Nakatsuka, Y.; Xue, Z.; Garcia, H.; Matsuoka, T. Experimental study on CO_2 monitoring and quantification of stored CO_2 in saline formations using resistivity measurements. *Int. J. Greenh. Gas Control* **2010,** *4*, 209– 216.

Oldenburg, C. M.; Moridis, G. J.; Spycher, N.; Pruess, K. *EOS7C Version 1.0: TOUGH2 Module for Carbon Dioxide or Nitrogen in Natural Gas (Methane) Reservoirs*; Report LBNL-56589; Lawrence Berkeley National Laboratory, Berkeley, CA, 2004.

Onishi, K.; Ishikawa, Y.; Yamada, Y.; Matsuoka, T. *Measuring electric resistivity of rock specimens injected with gas, liquid and supercritical CO_2*, SEG Technical Program Expanded Abstracts, 2006; pp 1480–1484.

Pruess, K.; Oldenburg, C. M.; Moridis, G. J. *TOUGH2 User's Guide Version 2*; Report LBNL-43134; Lawrence Berkeley National Laboratory, Berkeley, CA, 1999.

Pruess, K. *ECO2N: A TOUGH2 fluid property module for mixtures of water, NaCl, and CO_2*; Report LBNL-57952; Lawrence Berkeley National Laboratory, Berkeley, CA, 2005.

Ramirez, A.; Daily, W.; Labrecque, D.; Owen, E.; Chesnut, D. Monitoring an underground steam injection process using electrical-resistance tomography. *Water Resour. Res.* **1993,** *29*, 73–87.

Ramirez, A.; Newmark, R. L.; Daily, W. D. Monitoring carbon dioxide floods using electrical resistance tomography (ERT): sensitivity studies. *Journal of Environment Engineering Geophysics* **2003,** *8*, 187–208.

Scheibe, T. D.; Chien, Y. J. An evaluation of conditioning data for solute transport prediction. *Ground Water* **2003,** *41*, 128–141.

Slater, L.; Binley, A. M.; Daily, W.; Johnson, R. Cross-hole electrical imaging of a controlled saline tracer injection. *Pure Appl. Geophys.* **2000,** *44*, 85–102.

Tryggvason, A. *PStomo_eq: User manual*. Dept. of Earth Sciences, Uppsala University, Uppsala, Sweden, 2009.

Tuminaro, R. S.; Heroux, M.; Hutchinson, S. A.; Shadid, J. N. *Official Aztec User's Guide: Version 2.1*; Sand Report SAND99-8801J; Sandia National Laboratories, Albuquerque, NM, 1999, pp 63.

Zhang, K.; Wu, Y. S.; Pruess, K. *User's Guide for TOUGH2-MP – A Massively Parallel Version of the TOUGH2 Code*; Report LBNL-315E; Lawrence Berkeley National Laboratory, Berkeley, CA, 2008.

NRAP is an initiative within DOE's Office of Fossil Energy and is led by the National Energy Technology Laboratory (NETL). It is a multi-national-lab effort that leverages broad technical capabilities across the DOE complex to develop an integrated science base that can be applied to risk assessment for long-term storage of carbon dioxide (CO_2). NRAP involves five DOE national laboratories: NETL, Lawrence Berkeley National Laboratory (LBNL), Lawrence Livermore National Laboratory (LLNL), Los Alamos National Laboratory (LANL), and Pacific Northwest National Laboratory (PNNL).

Technical Leadership Team

Diana Bacon
Lead, Groundwater Protection Working Group
Pacific Northwest National Laboratory
Richmond, WA

Jens Birkholzer
LBNL Lab Lead
Lawrence Berkeley National Laboratory
Berkeley, CA

Grant Bromhal
Technical Director, NRAP
Research and Innovation Center
National Energy Technology Laboratory
Morgantown, WV

Chris Brown
PNNL Lab Lead
Pacific Northwest National Laboratory
Richmond, WA

Susan Carroll
LLNL Lab Lead
Lawrence Livermore National Laboratory
Livermore, CA

Abdullah Cihan
Lead, Reservoir Performance Working Group
Lawrence Berkeley National Laboratory
Berkeley, CA

Tom Daley
Lead, Strategic Monitoring Working Group
Lawrence Berkeley National Laboratory
Berkeley, CA

Robert Dilmore
NETL Lab Lead
Research and Innovation Center
National Energy Technology Laboratory
Pittsburgh, PA

Nik Huerta
Lead, Migration Pathways Working Group
Research and Innovation Center
National Energy Technology Laboratory
Albany, OR

Rajesh Pawar
LANL Lab Lead
Lead, Systems/Risk Modeling Working Group
Los Alamos National Laboratory
Los Alamos, NM

Tom Richard
Deputy Technical Director, NRAP
The Pennsylvania State University
State College, PA

Josh White
Lead, Induced Seismicity Working Group
Lawrence Livermore National Laboratory
Livermore, CA

Sean Plasynski
Executive Director
Technology Development and
Integration Center
National Energy Technology Laboratory
U.S. Department of Energy

Heather Quedenfeld
Associate Director
Coal Development and Integration
National Energy Technology Laboratory
U.S. Department of Energy

Traci Rodosta
Technology Manager
Strategic Planning
Science and Technology Strategic Plans
and Programs
National Energy Technology Laboratory
U.S. Department of Energy

Mark Ackiewicz
Director
Division of Carbon Capture and Storage
Office of Fossil Energy
U.S. Department of Energy

NRAP Executive Committee

Cynthia Powell
Executive Director
Research and Innovation Center
National Energy Technology Laboratory

Donald DePaolo
Associate Laboratory Director
Energy and Environmental Sciences
Lawrence Berkeley National Laboratory

Roger Aines
Chief Energy Technologist
Lawrence Livermore National
Laboratory

Melissa Fox
Program Manager
Applied Energy Programs
Los Alamos National Laboratory

George Guthrie
Chair, NRAP Executive Committee
Earth and Environmental Sciences
Los Alamos National Laboratory

Alain Bonneville
Laboratory Fellow
Pacific Northwest National Laboratory

Grant Bromhal
Technical Director, NRAP
Senior Research Fellow
Research and Innovation Center
National Energy Technology Laboratory

NRAP Technical Report Series